ARTICLE   **Open Access**

Multimodal selenium nanoshell-capped Au@mSiO$_2$ nanoplatform for NIR-responsive chemo-photothermal therapy against metastatic breast cancer

Thiruganesh Ramasamy[1,2], Hima Bindu Ruttala[1], Pasupathi Sundaramoorthy[3], Bijay Kumar Poudel[1], Yu Seok Youn[4], Sae Kwang Ku[5], Han-Gon Choi[6], Chul Soon Yong[1] and Jong Oh Kim[1]

Abstract

Multimodal therapeutic agents based on novel nanomaterials for multidrug resistance have attracted increasing attention in cancer therapy. In this study, we describe the construction of a programmed mesoporous silica-capped gold nanorod covered with nano-selenium overcoat (Se@Au@mSiO$_2$) nanoparticles as a multifunctional nanoplatform to incorporate materials with specific chemotherapeutic, chemoprevention, and photoablation/hyperthermia functions that collectively contribute to enhance anticancer efficacy in multidrug-resistant breast cancer. The triple-combination-based nanosized Se@Au@mSiO$_2$/DOX effectively accumulates in the tumor and the release of the therapeutic cargo could be remotely manipulated by mild near-infrared (NIR) irradiation. Se@Au@mSiO$_2$/DOX notably enhances the cell killing effect through induction of cell apoptosis. In addition, Se@Au@mSiO$_2$/DOX inhibits tumor cell growth through cell cycle arrest and induction of apoptosis via suppression of the Src/FAK/AKT signaling pathways. Synergistic Se-photothermal-chemotherapy combination exhibits significant tumor growth suppression and delayed tumor progression in vivo. Immunohistochemistry analysis shows elevated numbers of caspase-3 and PARP-immunolabeled cells and decreased Ki-67 + and CD31 + cancer cells in the tumor mass. No noticeable signs of organ damage or toxicity are observed after treatment with Se@Au@mSiO$_2$/DOX (NIR+), which is further supported by hematology and biochemical analyses. Thus, Se@Au@mSiO$_2$/DOX has potential for the clinical treatment of metastatic breast cancers with little or no adverse effects.

Introduction

Cancer is a worldwide problem with high rates of morbidity and mortality[1]. The clinical application of numerous broad-spectrum chemotherapeutic drugs has been hindered owing to severe toxicity at high doses to vital organs, including the liver, kidney, spleen, and lungs and immune system and ineffectiveness at low doses[2,3].

To improve the anticancer effects and overcome the side-effects, multiple anticancer agents or small molecules can be co-administered. However, the increasing prevalence of adjuvant drug administration has resulted in new side-effects and altered cachexia progression in cancer patients[4]. Furthermore, it has been difficult to integrate two drugs with different physicochemical characteristics onto a single carrier, and it has proven a tedious task to manipulate the ratiometric release of encapsulated compounds[5]. Given these setbacks, alternative strategies need to be employed to enhance therapeutic selectivity and reduce chemotherapeutic drug toxicity.

Correspondence: Han-Gon Choi (hangon@hanyang.ac.kr) or Chul Soon. Yong (csyong@ynu.ac.kr) or Jong Oh. Kim (jongohkim@yu.ac.kr)
[1]College of Pharmacy, Yeungnam University, 214-1, Dae-dong, Gyeongsan 712-749, Republic of Korea
[2]Department of Medicine, Center for Ultrasound Molecular Imaging and Therapeutics, University of Pittsburgh, Pittsburgh, PA 15213, USA
Full list of author information is available at the end of the article

Nanomedicine through metallic nanoparticles is emerging as a potential therapy in the treatment of cancers. Epidemiological studies, preclinical investigations, and clinical intervention trials suggest that co-delivery with selenium (Se) could decrease the toxicity of chemotherapeutic drugs, as well as prevent and reduce cancer incidence[6]. Numerous studies have suggested that Se supplementation could sensitize cancer cells towards antitumor agents and overcome multidrug resistance, effectively modulating the therapeutic efficacy and selectivity of anticancer drugs[7,8]. For example, Hu et al.[7] reported that Se enhanced the therapeutic efficacy of paclitaxel against prostate cancers. Se has been reported to improve the pharmacological properties of 5-fluorouracil in A375 melanoma cancers and exhibited a synergistic anticancer effect[9]. Rustum et al.[10] reported that the toxicity profile of taxol, 5-FU, cisplatin, and anthracycline decreased when combined with Se. Nano-Se inhibits tumor cell proliferation by blocking various signaling pathways, the induction of angiogenesis, and increases in reactive oxygen species (ROS) production that lead to mitochondria dysfunction[11].

The integration of multiple components into a nanocomposite with each material exhibiting its pharmacological activity in a coordinated way provides interesting and creative possibilities[12]. In recent years, near-infrared (NIR) light-responsive gold nanorods (AuNR) have received much attention as a potential anticancer treatment agent. NIR laser-mediated photothermal ablation (PTA) has been demonstrated to induce a hyperthermia effect in tumor cells by increasing the local temperature without any significant damage to surrounding healthy tissues[13,14]. The tumor ablation properties of AuNR have been attributed to its high optical and electronic properties that manifest itself efficiently during photothermal conversion in tumor therapy[15]. Nevertheless, the possibility of some tumor cells receiving inadequate laser exposure ultimately leads to low clinical efficacy, necessitating the need of multimodal anticancer nanomedicine[16]. The presence of multiple modalities would target different signaling pathways and thereby synergize the therapeutic outcome, and could effectively limit side-effects[17]. For example, Chan et al.[18] combined PTA (hyperthermia) with chemotherapy and reported 84 and 78% higher cell killing potency than PTA therapy alone and cisplatin, respectively. In this milieu, a carrier that can integrate all of the components, including Se, AuNR, and chemotherapeutic drugs (doxorubicin, DOX), is required. Among all potential carriers, mesoporous silica nanoparticles (MSN) were observed to fulfill the concept of 3-component-combinational therapy. The biomedical importance of MSN can be attributed to its large surface area, high accessible pore volume, tunable size, biocompatibility, and well-defined surface functionalization[19,20].

To develop new strategies for the effective treatment of breast cancer, we designed a novel anticancer nanomedicine agent by combining nano-Se, PTA, and chemotherapy. Towards this purpose, multimodal NPs (Se@Au@mSiO$_2$/DOX) were constructed, and the efficacy of Se@Au@mSiO$_2$/DOX nanocomposite-mediated combination therapy for the induction of cellular apoptosis and ROS generation to inhibit cancer cell proliferation and migration and to suppress the tumor burden was evaluated in vitro and in vivo using MDA-MB-231 breast cancer cells.

Materials and methods

Materials

Doxorubicin hydrochloride was a kind gift from Dong-A Pharmaceuticals, Korea. Chloroauric acid tetrahydrate (HAuCl$_4$·4H$_2$O), cyltrimethylammonium bromide (CTAB), tetraethoxysilane (TEOS), sodium borohydride (NaBH$_4$ >96%), 3-mercaptopropyltrimethoxysilane (MPTMS, 95%), silver nitrate (AgNO$_3$), ascorbic acid (AA), sodium selenite, and glutathione (GSH) were purchased from Sigma-Aldrich, Korea. All other chemicals were of reagent grade and used without further purifications.

Synthesis of CTAB-stabilized gold nanorods

AuNR were prepared by the seed-mediated method as previously reported by Sau and Murphy[21]. Briefly, the seed solution was prepared by adding 0.25 mL HAuCl$_4$ (0.01 M) and 7.5 mL CTAB (0.1 M) in a glass tube, followed by the addition of 0.6 mL ice-cold NaBH$_4$ and subsequent vortexing for 2 min. The solution was kept aside for 3 h at 25 °C in the dark. The growth solution was prepared by adding 0.2 mL HAuCl$_4$ (0.01 M) to 4.75 mL of CTAB (0.10 M), and 0.03 mL of AgNO$_3$ (0.01 M) solution was then added immediately. About 0.032 mL of AA was then added to the bright brown-yellow solution and vortexed for 20 s. Seed solution (0.02 mL) was added to the colorless solution and vortexed for 15 s. The solution was left undisturbed for at least 3 h in the dark.

Synthesis of mesoporous silica-coated gold nanorods (Au@mSiO$_2$)

The mesoporous silica coating on CTAB-stabilized AuNRs was generated by Stober's method with slight modifications[22]. Briefly, the AuNRs were washed to remove excess CTAB and dispersed in 1 mL of deionized water. About 200 μL of 0.2 M CTAB solution was added to the AuNR solution with gentle stirring. After 10 min, drops of 0.1 M NaOH were added to adjust the pH to 9. After 10 min, 300 μL of 17% TEOS (in ethanol) was added and the subsequent solution was gently stirred for 18 h.

Au@mSiO$_2$ was washed several times with water and methanol to remove excess CTAB. The obtained product was dried under vacuum.

Synthesis of *thiol*-modified Au@mSiO$_2$

First, a thiol group was introduced into Au@mSiO$_2$ nanocomposites. One-hundred milligram Au@mSiO$_2$ was dissolved in 20 mL of methanol and 0.2 mL of 3-mercaptopropyltrimethoxysilane was added. The mixture was stirred at 50 °C for 30 h. Au@mSiO$_2$-SH was separated by centrifugation and the nanocomposites were washed three times and dried.

DOX-loading in *thiol*-modified Au@mSiO$_2$

Au@mSiO$_2$-SH (100 mg) was dissolved in water with mild sonication. DOX solution (2 mL; 7.5 mg/mL) was added to the above solution and incubated for 18 h under mild agitation. After incubation, unentrapped DOX was removed by centrifugation and DOX-loaded Au@mSiO$_2$-SH (Au@mSiO$_2$/DOX) was re-dispersed in distilled water.

Synthesis of Se@Au@mSiO$_2$/DOX nanocomposite

Au@mSiO$_2$/DOX was dispersed in water in a glass tube and 10 mM GSH solution was added and vortexed for 10 s. Sodium selenite (10 mM) was immediately added and the solution pH was adjusted to 7.1. Nano-Se was condensed on the surface of thiol-modified Au@mSiO$_2$/DOX carriers, creating a Se overcoat. The final product Se@Au@mSiO$_2$/DOX was collected after centrifugation of the solution mixture and stored for further use.

Physicochemical characterizations of Se@Au@mSiO$_2$/DOX

Particle size and zeta potential were measured by the dynamic light scattering (DLS) technique using a Zetasizer Nano ZS (Malvern, UK) at 25 °C. The morphology of nanoparticles was studied by transmission electron microscopy (TEM; CM 200 UT; Philips, Andover, MA, USA) and atomic force microscopy (AFM; NanoScope IV system; Veeco, Santa Barbara, CA, USA). Solid state characterizations were performed using an X-ray diffractometer (X'Pert PRO MPD diffractometer, Almelo, Netherlands) and a differential scanning calorimeter (DSC-Q200, TA Instruments, New Castle, DE, USA). Sample pore characteristics were studied by determining nitrogen adsorption using a surface area and pore size analyzer (SA3100, Beckman coulter, USA) at −196 °C. MSNs were degassed at 350 °C for 12 h prior to analysis, while drug-loaded samples were degassed at 40 °C for 12 h. The specific surface area was calculated according to the Brunauer–Emmett–Teller (BET) theory. Pore size and volume were calculated by the Barrett–Joyner–Halenda (BJH) method according to the isotherm adsorption data. MSN surface element composition was determined by X-ray photoelectron spectroscopy (XPS) using an ESCALAB

MKII spectrometer (VG Co., United Kingdom). The energy-dispersive X-ray spectra (EDS) and SEM were inspected using a field emission scanning electron microscope (FESEM, S4800, Hitachi Co., Japan) equipped with an EDS (Jeol JXAe840). Small angle XRD patterns were collected in the range of 0.6–5 using Rigaku D/max-RA power diffraction-meter using Cu Ka radiation. The release study was performed by the dialysis method. The samples were packed in a dialysis membrane (MWCO 3500 Da) and placed in a release medium (phosphate-buffered saline, PBS [pH 7.4]) at 100 rpm at 37 °C. Samples were withdrawn at specific time points and the amount of DOX released was calculated by UV–Vis spectroscopy (Perkin Elmer U-2800, Hitachi, Tokyo, Japan). In addition, released samples were exposed to NIR laser light for 1–4 h using a High Power Fiber-Coupled Laser (Edmund Optics, China).

In vitro cytotoxicity assay and photothermal ablation experiment

An in vitro cytotoxicity assay was performed in MCF-7 and MDA-MB-231 breast cancer cells. The cells were cultured in Dulbecco's Modified Eagle's Medium (DMEM) media supplemented with 10% fetal bovine serum (FBS) and 1% penicillin-streptomycin in a humidified atmosphere of 5% CO$_2$ at 37 °C. To perform a cytotoxicity assay, 1×10^4 cells were seeded per well in a 96-well plate and incubated for 24 h. The cells were then treated with free DOX, nano-Se, Au@mSiO$_2$/DOX (with and without NIR) or Se@Au@mSiO$_2$/DOX (with and without NIR) and incubated for 24 h. After this, cells were carefully washed and treated with 100 μL of MTT solution (1.25 μg/mL) and incubated for an additional 4 h. Formazan was extracted by adding 100 μL of DMSO and kept aside for 30 min. The absorbance at 570 nm was measured using a microplate reader (Multiskan EX, Thermo Scientific, USA). The IC$_{50}$ value (the concentration that inhibits cell growth by 50%) was calculated using SPSS software 17.0 (Chicago, IL, USA). Untreated cells were used as control cells throughout in bioassay experiments.

For PTA, the same procedure as mentioned above was followed. After 2 h of cellular uptake, cells were exposed to NIR laser irradiation (808 nm) at a power output of 2 W/cm^2 for 4 min. After this, cells were incubated for the remainder of the standard time interval.

Intracellular uptake and localization of Se@Au@mSiO$_2$/DOX

The cellular uptake of Se@Au@mSiO$_2$/DOX was studied by flow cytometry cell sorting (FACS, BD Biosciences, USA). The cells were seeded in a 6-well plate and incubated overnight. The cells were then incubated with free DOX, Au@mSiO$_2$/DOX or Se@Au@mSiO$_2$/DOX for 2 h, washed gently with PBS, extracted, suspended in PBS, and evaluated using FACS.

Intracellular uptake was studied by means of confocal laser scanning microscopy (CLSM). The cells were seeded in a 6-well plate and incubated overnight. Following this, cells were then incubated with Se@Au@mSiO$_2$/DOX for 1 h in serum-free media. The cells were then washed carefully and fixed with 4% paraformaldehyde (PFA) and incubated for 15 min. Nuclei were stained with DAPI to track intracellular uptake while subcellular localization was tracked with Lysotracker Green®. Images were captured using CLSM (Nikon A1+, Japan).

Cell apoptosis and cell cycle analysis

To investigate cell apoptosis, 2×10^5 cells were seeded per well in a 6-well plate and incubated overnight. The cells were then treated with free DOX (1 µg/mL), nano-Se, Au@mSiO$_2$/DOX (with and without NIR) or Se@Au@mSiO$_2$/DOX (with and without NIR) and incubated for 20 h in a standard incubator. The next day, cells were washed, extracted, and re-suspended in 50 µL of PBS. The cells were stained with annexin-V/FITC and PI (2.5 µL each) and incubated for 15 min. Apoptotic cells were detected using FACS.

For cell cycle analysis, extracted cells were fixed in 70% ice-cold ethanol and kept at 4 °C for 24 h. The cells were then treated with RNAse A at 37 °C for 30 min and stained with PI for another 30 min under dark conditions. Cell cycle distribution was studied using FACS.

Measurement of intracellular reactive oxygen species (ROS) and oxidative stress level

Cells (2×10^5) were seeded in a 96-well plate and treated with the formulations (1 µg/mL DOX) for 4 h. The cells were then treated with control, free DOX, nano-Se, Au@mSiO$_2$/DOX (with and without NIR) or Se@Au@mSiO$_2$/DOX (with and without NIR) and incubated for 20 h. The cells were then extracted, washed twice with PBS, and incubated with 10 µM DCFH-DA at 37 °C for 30 min. ROS generation was then evaluated by FACS.

For intracellular oxidative stress levels, 2×10^4 cells were seeded in each well of a 96-well plate. The cells were washed and incubated with 50 µL of glutathione lysis reagent or oxidized glutathione lysis reagent for 5 min under gentle shaking. Followed this, 50 µL of luciferin generator solution was added and incubated for 30 min. Finally, 10 µL of luciferin detection reagent was added and equilibrated for 15 min. Intracellular reduced (GSH) and oxidized (GSSG) glutathione levels were measured using the Promega GSH/GSSG-Glo™ assay kit, and luminescence was measured using a luminometer (LMax II, Molecular Devices, Sunnyvale, CA, USA).

Cell migration assay

A cell migration assay was performed using an IncuCyte ZOOM™ system (Ann Arbor, Michigan, USA). For this purpose, 1×10^4 cells were seeded per well into a 96-well plate, allowed to incubate for 24 h, and then treated with respective formulations at 1 µg/mL and incubated for another 24 h. Cell monolayers were scratched and images of cell migration were captured using the IncuCyte ZOOM™ system. The migration rate was calculated with IncuCyte ZOOM™ software using the formula: percentage of scratch closure $= a - b/a \times 100$, where "a" is the distance between the edges of the wound and "b" is the distance that remained cell-free during wound closure.

Colony formation assay

Approximately 100–200 cells were plated per well in a 6-well plate and incubated overnight. The cells were then treated with free DOX (0.1 µg/mL), nano-Se, Au@mSiO$_2$/DOX (with and without NIR), or Se@Au@mSiO$_2$/DOX (with and without NIR). The media was changed every 3 days. After 14 days, visible colonies were fixed with methanol and stained with hematoxylin and eosin. The treatments within a single experiment and the entire experiment itself were performed in triplicate.

Immunoblot analysis

Cells were seeded in 6-well plates, allowed to incubate overnight, and then treated with respective formulations and incubated for 24 h. The cells were then washed, extracted, lysed, and protein was collected with M-PER® protein extraction reagent (Pierce, Rockford, USA). The protein concentrations were estimated using a standard BCA protein assay protocol (Pierce, USA). The proteins were then loaded onto a polyacrylamide gel and later transferred to nitrocellulose membranes (Bio-Rad). Membranes were blocked with 5% skim milk and then incubated with various cell-specific primary antibodies and incubated overnight. Next day, membranes were incubated with secondary antibody and bands were observed after exposing to Kodak-X-OMAT film for 10 s for data acquisition.

Biodistribution and in vivo antitumor efficacy studies

Female BALB/c nude mice (7-week-old) were procured from Orient Bio (Seoul, South Korea). The animals were handled as per the guidelines framed by the Institutional Authority for Laboratory Animal Care and Handling, Yeungnam University, South Korea. MDA-MB-231 tumor-bearing mice were prepared by injecting 1×10^7 cells (100 µL in Matrigel®) into the right flank of the mice. The tumors were allowed to grow until they reached 75–100 mm^3. The mice were divided equally into seven groups with eight mice in each group. The mice were intravenously administered respective formulations (free DOX [5 mg/kg], nano-Se, Au@mSiO$_2$/DOX [with and without NIR] and Se@Au@mSiO$_2$/DOX [with and without NIR]). Mice received four injections with a gap of

3 days between each injection. At 12 h after administration, the entire tumor region was exposed to NIR laser irradiation ($\lambda = 808$ nm) at a power output of 2 W/cm^2 for 5 min. During irradiation, thermographs were taken using a NIR camera (IRT Cronista, ThermApp®). The thermographs were analyzed using professional software to obtain the average temperature of the formulation at each time point. Tumor size was measured using Vernier calipers and the body weights of mice were recorded. Tumor volume (V_t), tumor growth rate (TGR), and tumor suppression rate (TSR) were calculated using the following formulas: $V_t = a \times b^2/2$; TGR (%) = (V_t/V_o) × 100%; TSR (%) = [(TGR$_c$ - TGR$_x$)/TGR$_c$] × 100%, where "a" and "b" represent tumor length and depth, respectively. V_0 and V_t represent the initial and final tumor volumes respectively. For the biodistribution analysis, the animals were intravenously administered Se@Au@mSiO^2 formulations when tumors reached approximately 800 mm^3 in volume. Cyanin 5.5 was used as a fluorescent probe to track the nanoparticle distribution in the body. The mice were sacrificed at 24 h after tail vein injection of nanoparticles, and the whole body was evaluated using an in vivo imaging apparatus (FOBI, NeoScience Co., Ltd, Seoul, South Korea). The tumor tissues and main organs (the heart, liver, spleen, lung, and kidney) of each animal were harvested for nanoparticle distribution analysis.

Evaluation of acute toxicity

Healthy female BALB/c nude mice (7-week-old) were divided into seven groups with five mice in each group. MDA-MB-231 tumor-bearing mice were prepared by injecting 1×10^7 cells (100 μL in Matrigel®) into the right flank of the mice. The tumors were allowed to grow until they reach 75–100 mm^3. The mice were administered respective formulations as mentioned above and monitored every day for any adverse reactions or activities. Seven days after injection, blood was collected in heparinized tubes and stored at 4 °C until further analysis. The serum was isolated from whole blood and subjected to testing for clinically important biochemical parameters such as ALT, AST, BUN, TBIL, and CR. In addition, RBC, HB, WBC, and PLT counts were evaluated.

Histopathological and immunohistochemical analysis

The tumor mass and vital organs (heart, liver, kidney, spleen, and lung) were surgically removed, fixed in 10% formalin, sliced, and embedded in paraffin. The tumor and organ samples were stained with H&E and evaluated under a light microscope (Nikon, Tokyo, Japan) for the detection of histological changes. Immunoreactivity to Ki-67, CD31, caspase-3, and PARP were analyzed with primary monoclonal antibodies. DNA fragmentation was determined by TUNEL assay using an in situ Apoptosis Detection kit (ab206386, Abcam Inc., Cambridge, MA, USA).

Statistical analysis

All data are presented as the mean ± standard deviation (SD). Means of treatment groups were compared using Student's *t*-test (SPSS Version 17; IBM, SPSS, Bethesda, MD, USA). A *p*-value < 0.05 was considered significant.

Results and discussion

Synthesis and characterization of Se@Au@mSiO$_2$/DOX

Herein, a novel nanoplatform was designed by assembling nano-Se on the surface of NIR-responsive Au@mSiO$_2$/DOX nanoparticles for the effective treatment of metastatic breast cancer (Se@Au@mSiO$_2$/DOX, Fig. 1). During NIR irradiation, the surface plasmon resonance (SPR) property of the AuNR would act as a localized heat source and exhibit a photothermal effect. AuNR would efficiently convert NIR light into local heat and induce tumor ablation. NIR-induced hyperthermia will trigger accelerated drug release in the tumor tissues[23]. Nano-Se could sensitize cancer cells towards antitumor agents and overcome multidrug resistance. The AuNR was synthesized by a seed-mediated method with an aspect ratio of 4.5 with approximately 40 nm in length and 9 nm in width as determined by TEM examination (Fig. 2a). TEM showed a typical rod-like shape for AuNR while mesoporous silica shells capped AuNR. Au@mSiO$_2$ particles were perfectly spherical with uniform dispersity. The mesoporous silica shells of Au@mSiO$_2$ would act as a drug/cargo reservoir. Nano-Se deposition did not alter the shape of Au@mSiO$_2$ and formed a thin layer as depicted by TEM examination. Three-dimensional imaging of particles was observed by AFM (Fig. 2b). AFM imaging revealed a broader particle for Se@Au@mSiO$_2$/DOX, which was uniformly flattened on the mica surface. The AuNR exhibited a SPR peak at 775 nm (Supplementary Fig. S1). The absorption band of Au@mSiO$_2$ showed a slight red shift (5 nm) upon silica assembly and after nano-Se deposition on top of Au@mSiO$_2$ due to the local increase in refractive index. The successful assembly of silica was further confirmed by zeta potential measurement. The AuNR exhibited a high-positive surface charge (+30 mV) due to the presence of CTAB on the surface (Figure S2). Silica assembly switched the surface charge to slightly negative, indicating a successful coating. The surface charge further changed to a strong negative upon deposition of nano-Se. The final size of Se@Au@mSiO$_2$/DOX was around 100 nm with a narrow polydispersity index (Fig. 2c), which was suitable for the targeting of tumor tissues via the EPR effect[24,25]. In addition, the nanosystem showed a high entrapment efficiency of >90% with an active drug loading of 8.1 ± 1.5% w/w.
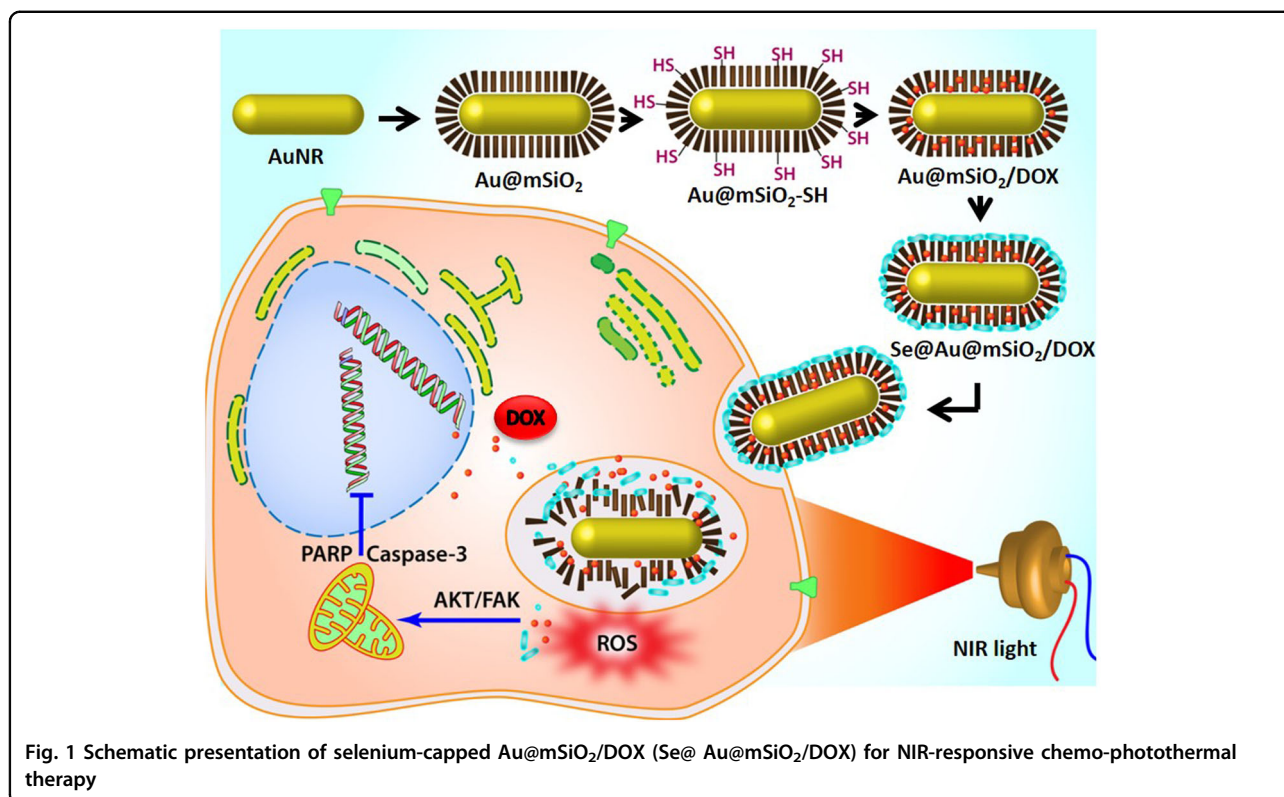
Fig. 1 Schematic presentation of selenium-capped Au@mSiO₂/DOX (Se@ Au@mSiO₂/DOX) for NIR-responsive chemo-photothermal therapy

Drug incorporation was further confirmed by X-ray diffraction (Supplementary Fig. S3). Free DOX exhibited multiple diffraction peaks corresponding to its crystalline nature, while no such characteristic peaks were observed in Au@mSiO$_2$/DOX or Se@Au@mSiO$_2$/DOX, indicating the presence of drug in the amorphous or in the molecular state in the nanocomposite. The drug incorporation was further analyzed by UV–Vis spectra (Supplementary Fig, S4), which clearly showed the drug loading capacity of Au@mSiO$_2$. The first spectra were the DOX spectra from the supernatant solution while the second spectra were that of the drug-loaded nanoparticles. Similarly, DSC showed a sharp endothermic peak at 195 °C corresponding to its melting point and crystalline nature (Supplementary Fig. S5). The absence of any such endothermic peak was attributed to the molecular insertion of the small molecules in the nanocarriers[26,27]. The stability of Au@mSiO$_2$/DOX and Se@Au@mSiO$_2$/DOX was studied in FBS-containing PBS buffer. No significant change in particle size was observed after 30 days of storage, indicating its excellent dispersion and stability.

To demonstrate the potential application of Se@Au@mSiO$_2$/DOX in chemo-photothermal therapy, nanoformulations were exposed to NIR laser irradiation at 808 nm with a power density of 2 W/cm² for 5 min. A linear correlation between laser irradiation and temperature of colloidal solution was established. The temperature of Se@Au@mSiO$_2$/DOX significantly increased compared to that of PBS control, suggesting the good potential of Se@Au@mSiO$_2$/DOX for PTA applications (Fig. 2d). Laser irradiation-mediated drug release was monitored using a UV–Vis spectrometer. It was observed that minimal amounts of DOX was released in the absence of laser irradiation (~10%), indicating that premature drug release in physiological conditions could be potentially inhibited (Fig. 2e). Upon irradiation, however, incremental release of DOX was observed with ~30% of drug released in 2 h and ~80% of drug released within 4 h of irradiation. The NIR laser increased the local heat of AuNR causing the drug to release from the pores of mesoporous silica. The laser-induced hyperthermia effect of Se@Au@mSiO$_2$/DOX could accelerate chemo-photothermal therapy. The anticancer drug (DOX) was loaded into the mesopores. DOX (ZP~ + 2.2 mV) could attach strongly to silica (ZP ~ −35 mV) through the charge interactions with silanol group surfaces. With external NIR laser stimulation, the Se@Au@mSiO$_2$ internalized within cancer cells induced local hyperthermia, endosomal disruption, rapid drug release, and enhanced cancer cell killing. Drug-encapsulated NPs showed a controlled release induced by NIR laser-induced hyperthermia. NIR photothermal agents, such as gold
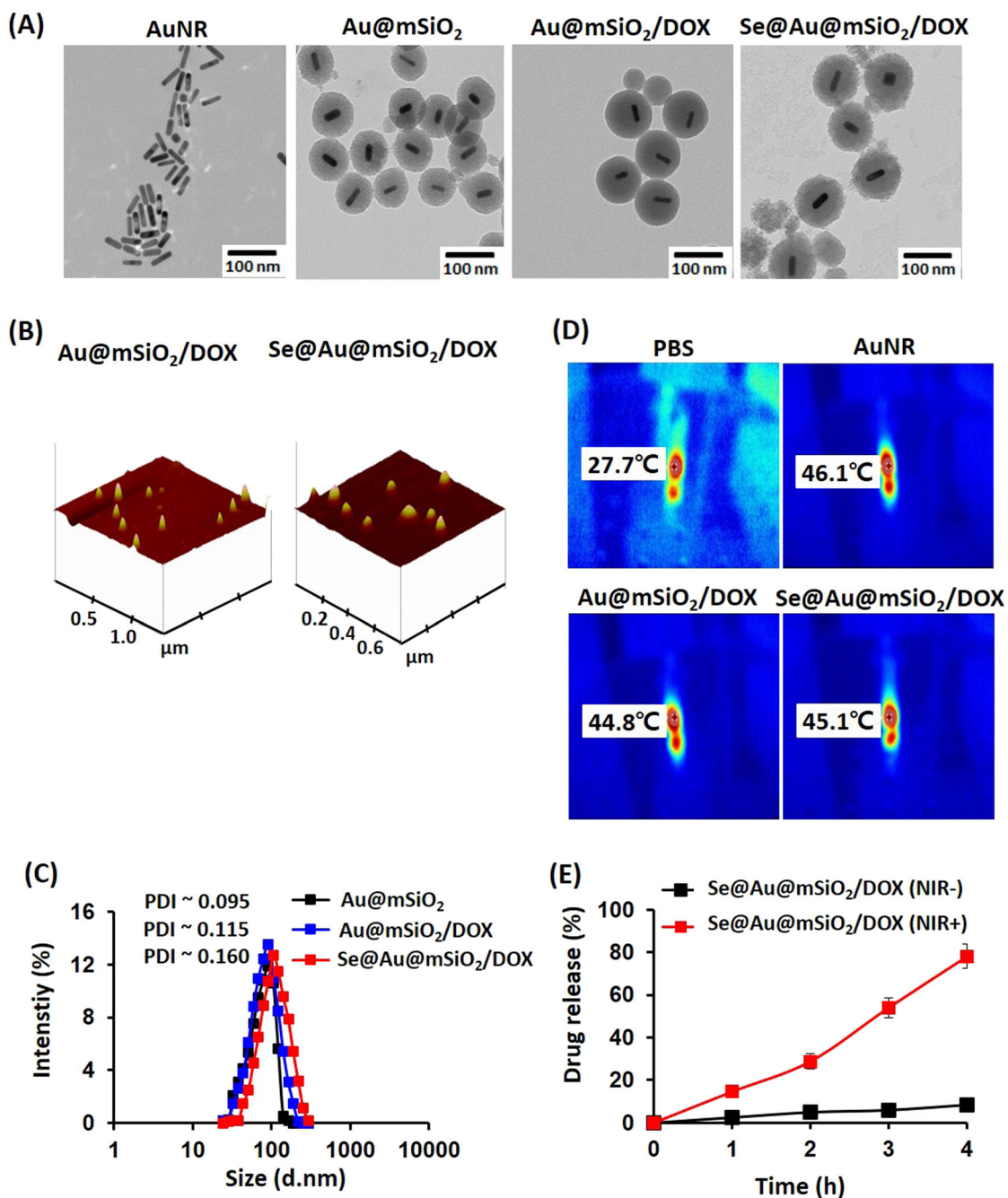
Fig. 2 Physicochemical characterization of Se@Au@mSiO₂/DOX. a TEM images of AuNR, Au@mSiO₂, Au@mSiO₂/DOX, and Se@Au@mSiO₂/DOX; **b** Three-dimensional AFM images of Au@mSiO₂/DOX, and Se@Au@mSiO₂/DOX; **c** DLS characterization of change in particle size upon each functionalization step; **d** thermographs of AuNR, Au@mSiO₂/DOX, and Se@Au@mSiO₂/DOX formulations after irradiation with NIR laser for 5 min. PBS was used as control; **e** in vitro drug-release profile of DOX from Se@Au@mSiO₂/DOX in the presence and absence of NIR irradiation (808 nm, 2 W/cm² for 5 min). The release was carried out at 37 °C in phosphate-buffered saline (pH 7.4) and data are shown as mean ± SD ($n = 3$)

nanorod, could strongly absorb the NIR laser and induce adequate temperature increase for triggering rapid drug release. The bond strength typically decreases with temperature increases, subsequently weakening the interaction between drug molecules and nanocarriers. Another possible factor could be that DOX molecules also present weak NIR absorbance, and thus, NIR irradiation accelerates its vibration and release.

The surface characterizations, including surface area, pore volume, and pore radius, were performed using

QuadraSorb Station 2. The MSN nitrogen adsorption/ desorption isotherms calculated by the BET theory were typical type IV isotherms according to the IUPAC classification, characteristic of mesoporous materials, with an inflection of capillary condensation observed at a P/P_0 value of about 0.8 for adsorption isotherms (Fig. 3a). It was observed that all MSN samples had high SBET (surface area) and pore volumes, indicating its potential application as a host in bonding or storing additional drug molecules in the drug-release system. Furthermore, the results showed that SBET and pore volume decreased after Se condensation and attachment on MSN surfaces. However, despite the reduction in nitrogen adsorption, the shape of the hysteresis loop remained unchanged. This meant that the pore shape was not significantly altered by the post synthesis approach, a fact that was in agreement with TEM analysis. Accordingly, specific surface area, cumulative pore volume and mean pore diameter were calculated before and after the Se adsorption procedure. The average pore radius of Au@MSN was 19.26 A°, pore volume was 1.01 cc/g, and the calculated surface area was 480.7 m^2/g, whereas all three parameters decreased after Se capping on the MSN surface. A significant difference in Se valency before and after assembly on the MSN surface was observed in the XPS patterns of Se *3d* and *3p* orbitals (Fig. 3b). Importantly, typical Se *3d* peaks of Se(IV) were detected at 59.5 eV and smaller peaks at 63 eV, while Se *3d* peaks of Se (0) were observed only at 63 eV, confirming the change in Se valence state in nanoparticle formulations. A similar change in valency for Au in the elemental state and the nanoparticle formulation was also observed (Supplementary Figs. S6 and S7). Small angle X-ray diffraction was performed to further confirm the difference in MSN surface before and after Se deposition (Supplementary Fig. S8). The data revealed that Se capping led to an obvious decrease in the intensity of the (100) XRD peak, similar to that of the surface area and pore diameter of MSN. As shown, the as-prepared MSN nanoparticles exhibited typical mesoporous structure patterns with a characteristic (100) peak at 1.85 (2Θ). After Se capping, a relatively weak peak at 1.92 could be found. Elemental microanalysis via energy-dispersive X-ray spectroscopy (EDS) was performed to identify the component elements of the composite nanoparticles (Fig. 3c). EDS revealed that Se@Au@mSiO2 contained 5.21 wt% of Au, 1.44 wt% of Se, and 16.35 wt% of Si, with high presence of C and O atoms, further verifying the successful construction of the composite nanoparticles.
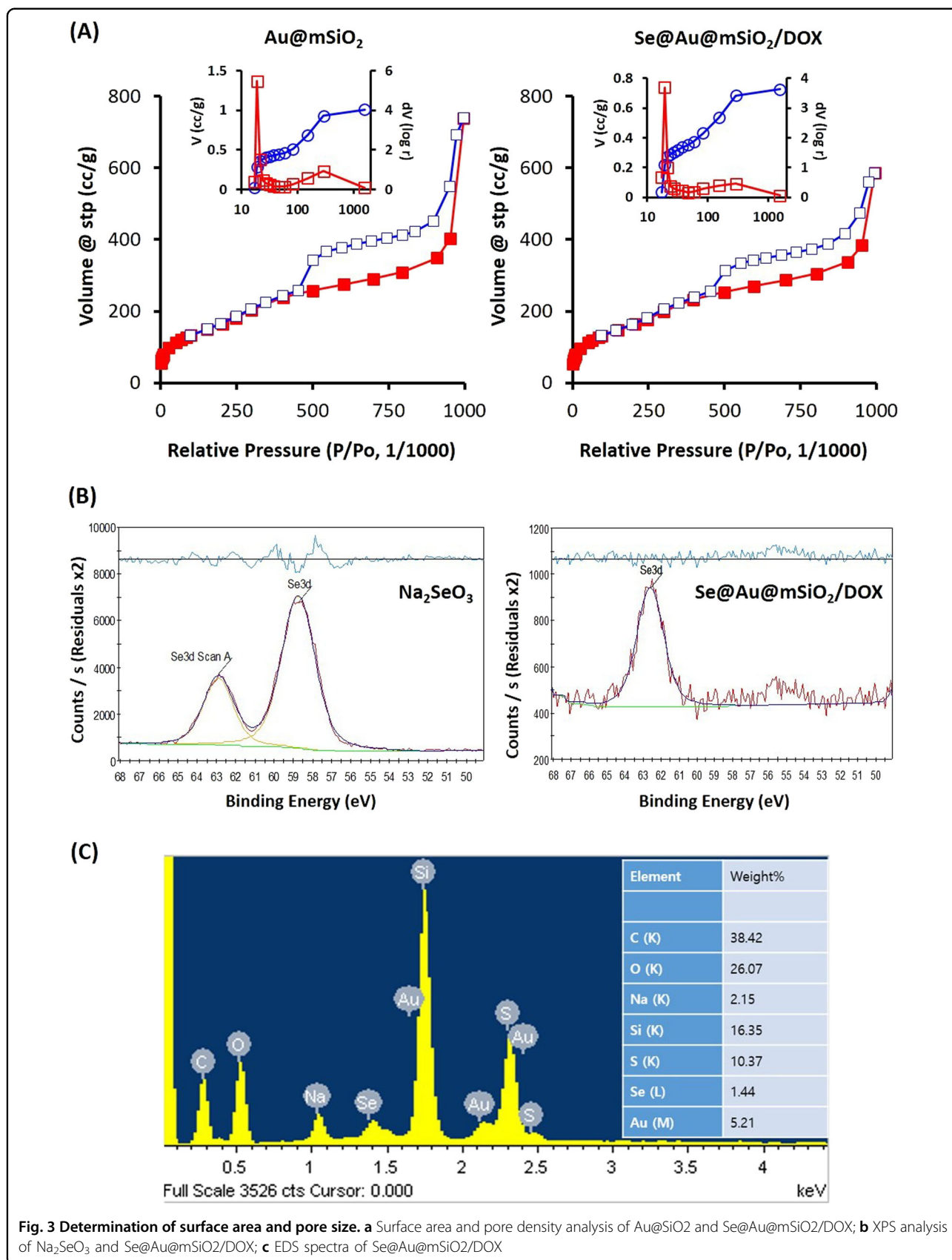
Intracellular uptake and subcellular distribution of Se@Au@mSiO2/DOX

Intracellular uptake of Se@Au@mSiO2/DOX was studied using flow cytometry (Fig. 4a). Cellular uptake of Se@Au@mSiO2/DOX was statistically lower than that of free DOX in MCF-7 cells ($p < 0.05$), however, nanocarriers showed comparable uptake in MDA-MB-231 cancer cells. This implies that the presence of the outer nano-Se shell did not affect the cellular uptake of the carrier and DOX accumulation in the cancer cells. The accumulation of free DOX significantly decreased in resistant MDA-MB-231 cells as overexpression of the p-gp receptor impeded cellular accumulation. These results indicated that the nanocarrier-based formulations effectively avoided p-gp-mediated efflux, thus offering an approach for reversing multidrug resistance (MDR)[28]. Intracellular DOX delivery was further confirmed by CLSM. As shown in Fig. 4b, a bright red fluorescence was observed in the cellular cytoplasm with no obvious nucleus accumulation after 2-h incubation, implying a typical endocytosis-mediated cellular internalization. Furthermore, the subcellular distribution of Se@Au@mSiO2/DOX was studied after staining the lysosome with LysoTracker Green®. DOX fluorescence was mainly located in the cytoplasmic region, and merged well with the green fluorescence denoting lysosomes. This indicated that DOX was present in the lysosomes and was released in a gradual manner (Fig. 4c). Based on these findings, Se@Au@mSiO2/DOX was initially located in the acidic organelles (late endosome-lysosome), and drug release occurs after nanoparticle destabilization[29]. Intracellular drug release in lysosomes will greatly enhance the efficacy of cancer treatment[30].

Synergistic analysis and chemo-photothermal analysis

To explore the synergistic effect of Se with chemotherapy and photothermal therapy, DOX, Au@mSiO2/DOX, and Se@Au@mSiO2/DOX were exposed to MCF-7 and MDA-MB-231 cancer cells. The AuNR-containing formulations were exposed to a NIR laser (808 nm, 2 W/ cm^2 for 4 min) and cell viability was evaluated by MTT assay (Fig. 5a). All of the formulations exhibited a typical dose-dependent cytotoxicity. Free DOX, which permeates the cell by simple diffusion, exhibits a cell killing effect by entering the nucleus and intercalating the DNA. The nanocarrier-based Se@Au@mSiO2/DOX exhibited a higher cytotoxic effect than the free drug owing to its superior permeability and cellular internalization characteristics[31]. The SeNP alone exhibited a broad-spectrum anticancer effect against MCF-7 and MDA-MB-231 cancer cells with IC_{50} values > 50 µg/mL. The synergistic effect of Se was visible when cancer cells were exposed to Se@Au@mSiO2/DOX. After NIR exposure, Se@Au@mSiO2/DOX showed a notably enhanced cell killing effect at equivalent concentrations vs. the other groups. The IC_{50} value of free DOX was considerably decreased with the synergistic combination of Se (sixfold) while NIR treatment (tenfold) further decreased the IC_{50} value, implying the importance of triple therapy in cancer

Fig. 3 Determination of surface area and pore size. a Surface area and pore density analysis of Au@SiO2 and Se@Au@mSiO2/DOX; **b** XPS analysis of Na_2SeO_3 and Se@Au@mSiO2/DOX; **c** EDS spectra of Se@Au@mSiO2/DOX
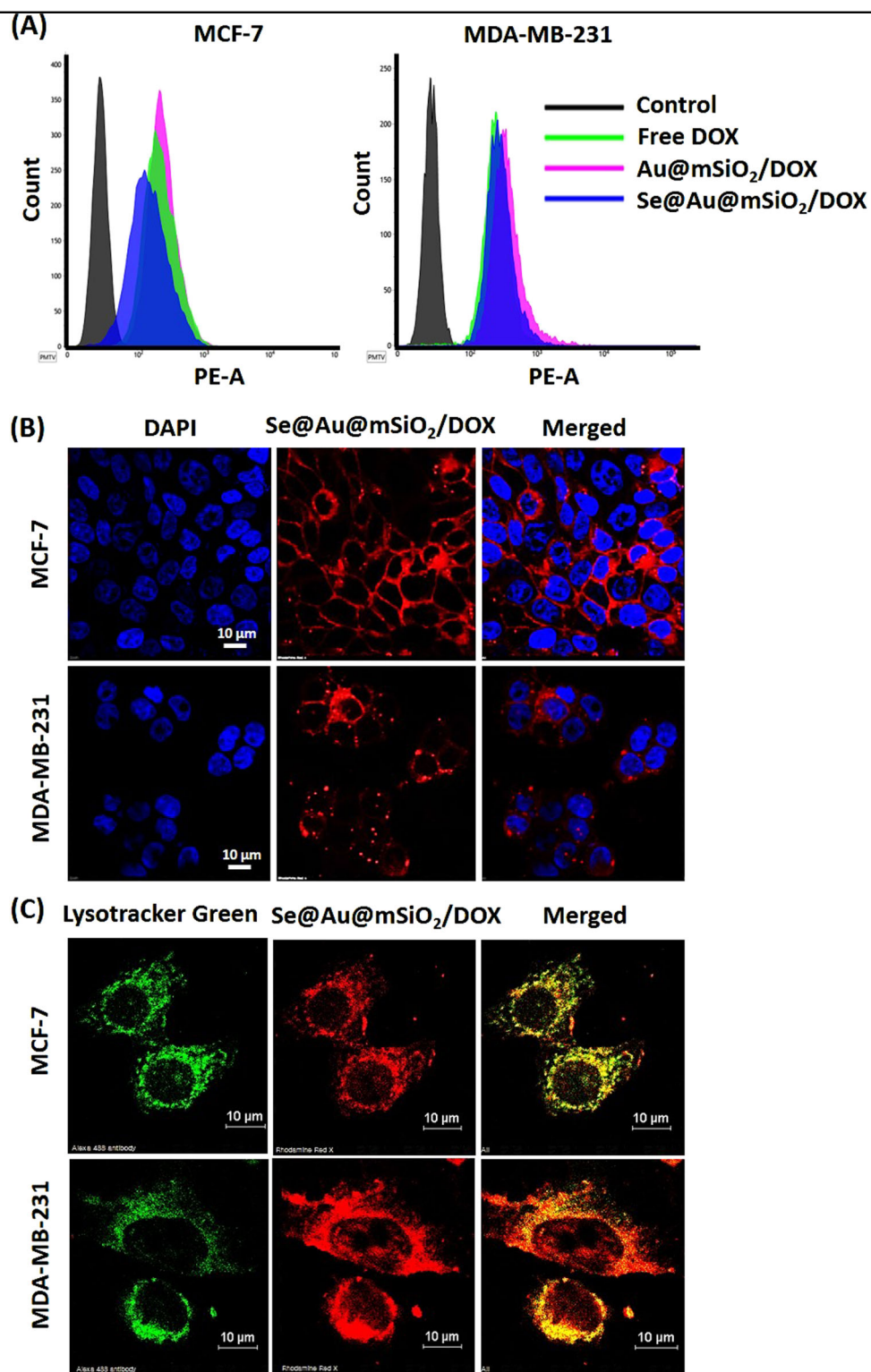
Fig. 4 Intracellular uptake and localization. a Comparative cellular uptake of free DOX, Au@mSiO$_2$/DOX, and Se@Au@mSiO$_2$/DOX in MCF-7 (sensitive) and MDA-MB-231 (resistant) cancer cells after 1 h of incubation; **b** intracellular uptake of Se@Au@mSiO$_2$/DOX in MCF-7 and MDA-MB-231 cancer cells (nuclei were stained with DAPI); **c** subcellular distribution of Se@Au@mSiO$_2$/DOX in MCF-7 and MDA-MB-231 cancer cells after lysosome staining with Lysotracker Green. DOX itself was used as a fluorescent probe and cell nuclei were stained with DAPI (blue). The formulation was incubated for 1 h and observed using CLSM
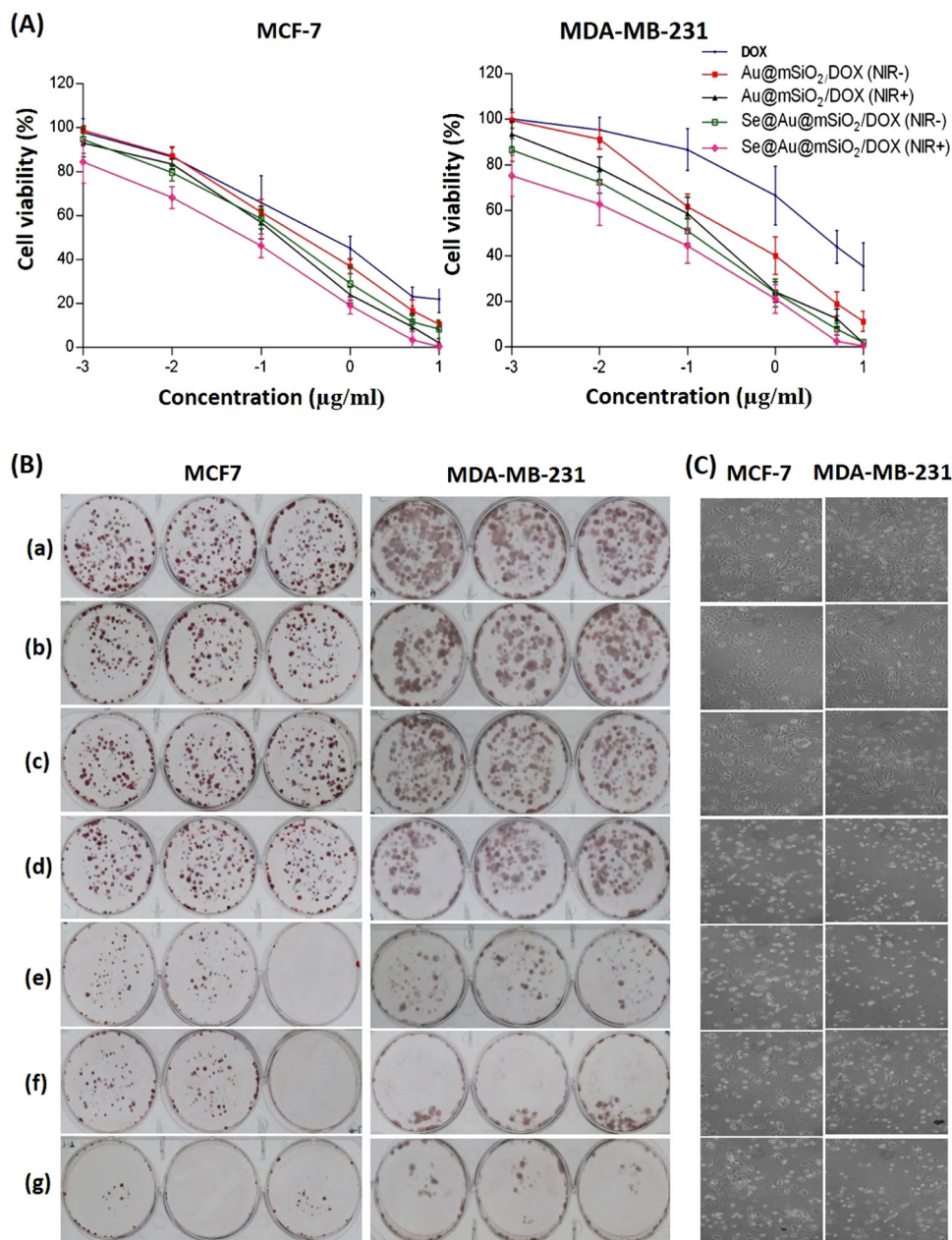
Fig. 5 In vitro cytotoxicity assay. a In vitro cytotoxic effects of free DOX, Au@mSiO$_2$/DOX (NIR±), and Se@Au@mSiO$_2$/DOX (NIR±) in MCF-7 and MDA-MB-231 cancer cells; **b** colony formation pattern and **c** morphological images of MCF-7 and MDA-MB-231 cancer cells after treatment with different formulations. **a** Control, **b** DOX, **c** Nano-Se, **d** Au@mSiO$_2$/DOX (NIR-), **e** Au@mSiO$_2$/DOX (NIR+), **f** Se@Au@mSiO$_2$/DOX (NIR-), and **g** Se@Au@mSiO$_2$/DOX (NIR+). The images for colony formation were observed at 10 × of fluorescence microscope

treatment. The triple-combination-based Se@Au@mSiO$_2$/DOX decreased the IC$_{50}$ value of DOX from 3.21 µg/mL to 0.085 µg/mL in MDA-MB-231 cancer cells, indicating the synergistic effect of all of the components in the nanocomposite. The cytotoxic effects of different nanoformulations were also observed through changes in cell morphology (Fig. 5b). Cell shrinkage, chromatin condensation and degeneration, and nuclear

fragmentation were observed in Se@Au@mSiO$_2$/DOX-treated cells, confirming its significant cytotoxicity[32]. Our results clearly showed that employing Se as an integral component of a nanosystem could be a highly efficient way to enhance anticancer efficacy. Simultaneously, the application of a NIR laser further improved the overall anticancer effect, demonstrating the synergistic effects of Se-chemo-photothermal treatment.

The superior anticancer effect of nanoformulations was further confirmed by a colony forming assay (Fig. 5c). The colony formation assay is based on the ability of a few cancer cells to grow into colonies under the influence of therapeutic agents. At an equivalent drug concentration, Se@Au@mSiO$_2$/DOX showed significant inhibition of colony formation compared to either free DOX or nano-Se. The significant decrease in the number of colonies was believed to be due to enhanced accumulation of Se@Au@mSiO$_2$/DOX, a synergistic effect of Se, and/or NIR-induced organelle damage, which was sufficient to kill cancer cells.

In vitro cell apoptosis and cell cycle distribution

Apoptosis has been reported to be one of main mechanisms of action for DOX and Se. Therefore, the synergistic effects of Se-chemo-photothermal therapy in MCF-7 and MDA-MB-231 cells were confirmed by an apoptosis assay using Annexin-V/PI staining. As shown in Supplementary Fig. S9, DOX induced nearly 20% apoptosis in MDA-MB-231 cancer cells, while Au@mSiO$_2$/DOX increased the percentage of apoptotic cells. Consistent with the results of the MTT assay, Se@Au@mSiO$_2$/DOX induced a significant increase in total apoptotic MDA-MB-231 cells (with 50% in early and ~10% late apoptosis). Among all the examined experimental groups, NIR-induced Se@Au@mSiO$_2$/DOX exerted the most significant therapeutic effect with almost ~40% of cells in late apoptosis, indicating its ability to reverse multidrug resistance.

It is believed that DOX and Se exert their pro-apoptotic effects by inducing changes in DNA fragmentation. Therefore, apoptotic cell death was further confirmed by PI-flow cytometric analysis (cell cycle distribution) (Supplementary Fig. S9). In general, cell cycle distribution following DNA damage is controlled by checkpoints. The failure to repair DNA could result in mitotic dysregulation and lead to cancer cell apoptosis[33,34]. Our results indicated that co-treatment with DOX and Se resulted in pronounced G2/M phase arrest in MDA-MB-231 cancer cells. Accordingly, the fraction of G1 cells continuously decreased proportionately to G$_2$/M phase arrest. Consistent with the apoptosis assay, Se@Au@mSiO$_2$/DOX induced a remarkable accumulation of cells in the sub-G0 phase (~80%). These results further confirm that apoptosis is the prime mechanism of action for Se, and that NIR exposure increased the proportion of apoptosis cells (sub-G0) due to the synergistic activity of multiple components.

Se@Au@mSiO$_2$/DOX induced mitochondrial dysfunction via ROS production

During oxidative metabolism, ROS are produced as a result of the mitochondrial respiratory chain reaction[35].

ROS play an important role in cell death pathways by regulating several key intracellular elements, and the overproduction of ROS activates various apoptotic signaling pathways. As shown in Fig. 6a and Supplementary Fig. S10, free DOX has a limited effect on ROS production, while Se@Au@mSiO$_2$/DOX significantly increased ROS generation in both MDA-MB-231 and MCF-7 cancer cells. Accordingly, NIR exposure further increased ROS generation, suggesting the involvement of this process in cellular apoptosis. The combination of anticancer agents and Se resulted in enhanced oxidative damage to mitochondria, which eventually resulted in apoptosis. ROS-mediated cell apoptosis was further confirmed by measurement of intracellular oxidative stress levels. Intracellular GSH, which is a major thiol, is essential for maintaining redox balance in cancer cells, and a decrease in the ratio of GSH/oxidized GSSG is an important index of oxidative stress and DNA damage[36]. As shown in Fig. 6b and Supplementary Fig. S11, free DOX, as well as Au@mSiO$_2$/DOX, has limited effects on the GSH/GSSG ratio, whereas Se, a ROS generating agent, significantly reduced the ratio, indicating severe oxidative stress. Accordingly, a combination of Se with Au@mSiO$_2$/DOX remarkably reduced the GSH/GSSG ratio, with the addition of NIR light further increasing the oxidative stress in cancer cells. The combination of anticancer agents, Se, and NIR-based PTA elevated intracellular ROS levels, leading to excessive oxidative stress, damage to intracellular components, and possible cellular apoptosis.

Cell migration analysis

Keeping in mind that cell migration plays an important role in tumor angiogenesis, we evaluated the inhibitory capacity of individual formulations on cell migration using a wound healing assay (Fig. 6c, Supplementary Fig. S12). Untreated cells retained their migration capacity, and the scratch was completely healed within 24 h in MDA-MB-231 and MCF-7 cancer cells. Free DOX (~10%) and free nano-Se (~5%) had limited effects in controlling wound closure, while Au@mSiO$_2$/DOX (~50%) was relatively more effective in reducing the migratory capacity of cancer cells (Supplementary Fig. S13). Most remarkably, Se@Au@mSiO$_2$/DOX showed the maximum anti-migratory effect (~80%), with the majority of cells either apoptotic or dead, indicating that a combination of Se with anticancer agents could synergize the anticancer effect. Accordingly, NIR exposure of Se@Au@mSiO$_2$/DOX displayed an even higher inhibition effect on the migration of MDA-MB-231 and MCF-7 cancer cells after 24 h incubation. The result further confirms that the triple-combination therapeutic strategy might be effective in suppressing tumor angiogenesis.
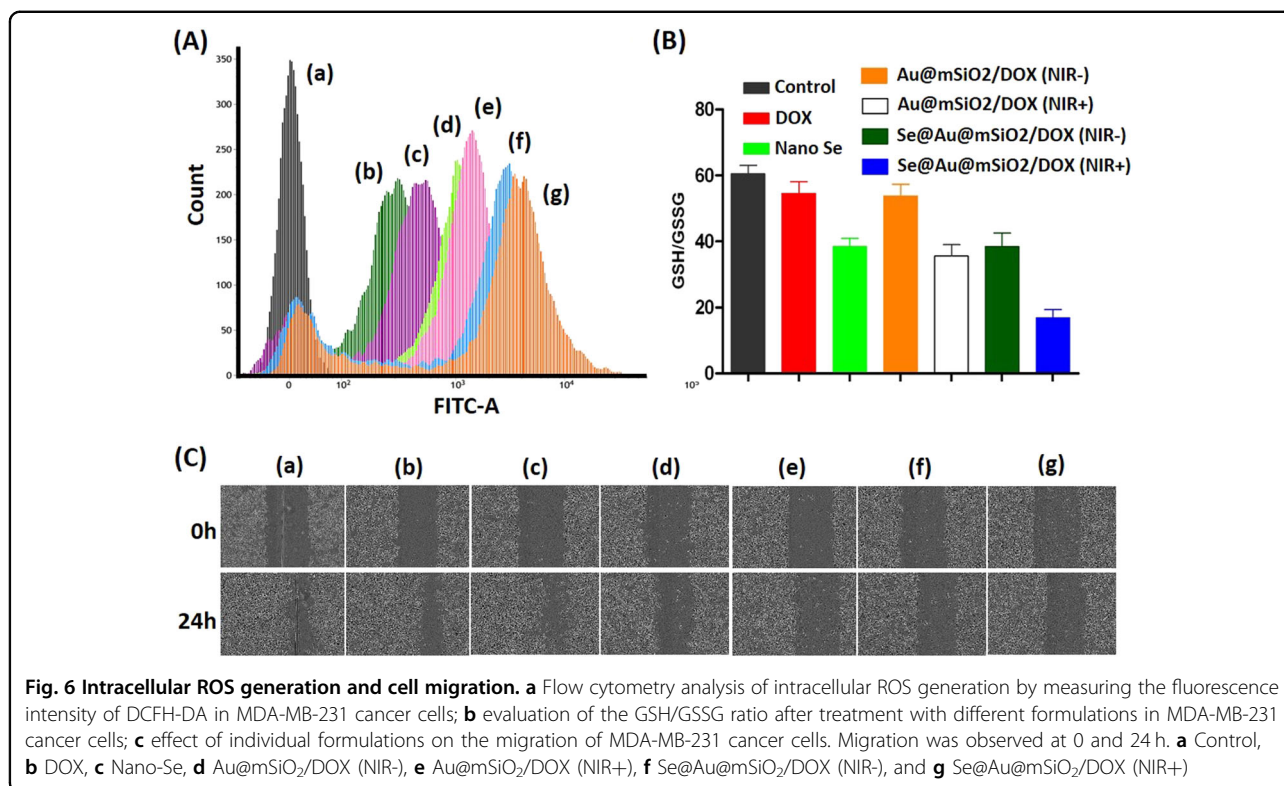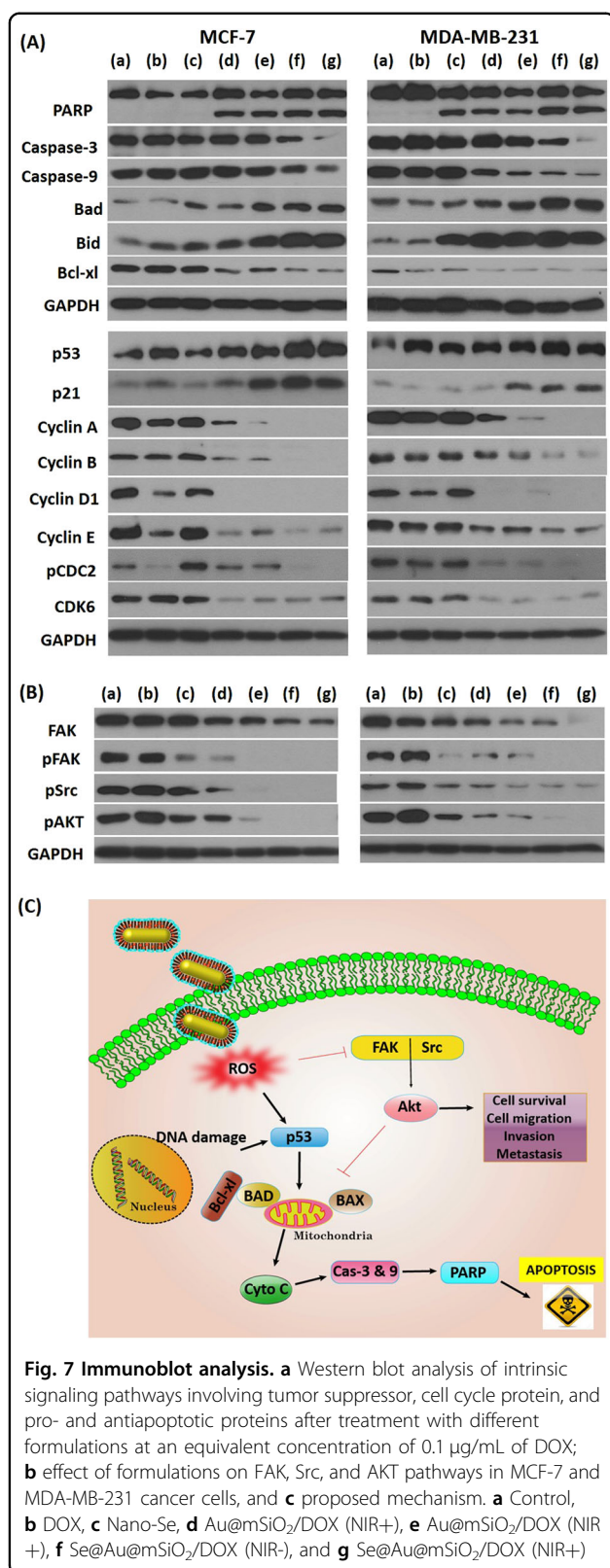
Fig. 6 Intracellular ROS generation and cell migration. a Flow cytometry analysis of intracellular ROS generation by measuring the fluorescence intensity of DCFH-DA in MDA-MB-231 cancer cells; **b** evaluation of the GSH/GSSG ratio after treatment with different formulations in MDA-MB-231 cancer cells; **c** effect of individual formulations on the migration of MDA-MB-231 cancer cells. Migration was observed at 0 and 24 h. **a** Control, **b** DOX, **c** Nano-Se, **d** Au@mSiO$_2$/DOX (NIR-), **e** Au@mSiO$_2$/DOX (NIR+), **f** Se@Au@mSiO$_2$/DOX (NIR-), and **g** Se@Au@mSiO$_2$/DOX (NIR+)

Regulation of intracellular apoptotic signaling pathways

Cancer therapy initiated by DNA damage is one of the effective strategies at the clinical level. In general, DOX exhibits its anticancer action through DNA intercalation, while apoptosis induction is considered to be the main mechanism of action for Se. ROS (generated from NIR exposure and Se) have been identified as a key intracellular component, which can regulate apoptotic signaling pathways and cell apoptosis[37]. Therefore, we performed a detailed western blot analysis to investigate the role of individual intracellular components and the synergistic effects of Se@Au@mSiO$_2$/DOX (Fig. 7a). A number of reports have cited that anticancer agents or ROS-mediated DNA damage could result in cell death via various apoptotic signaling pathways such as p53, AKT, or MAPK[37]. The phosphorylation of p53, which is an important tumor suppressor protein, controls the transcription of various genes that regulate cell arrest and apoptosis. Western blot analysis revealed that free DOX or Se did not affect the expression of p53. However, a combination of Se-chemo-photothermal effects (Se@Au@mSiO$_2$/DOX) resulted in marked upregulation of p53 and p21 expression in both cancer cell lines. p53-mediated transcription is considered important for the maintenance of cell cycle arrest, and the p21 protein inhibits the cyclin E-Cdk2 and cyclin D-Cdk4 complexes, thereby suppressing the Rb/E2F pathway and cell death. Damaged DNA activates Chk1, which in turn targets the

phosphatase Cdc25a for degradation, leading to the failure of Cdk2 activation[38,39]. Cell cycle analysis clearly showed that G2/M phase arrest, followed by an increase in sub-G0 peaks, was the main pathway for cell death. Therefore, we studied the internal mechanism that regulates cell cycle checkpoints. The results revealed that expression levels of the cell cycle regulators cyclin A, cyclin B, cyclin D1, and cyclin E were all remarkably downregulated by Se@Au@mSiO$_2$/DOX compared to treatment with the individual components (free DOX and Se). All these cyclins are intrinsically involved in controlling apoptosis levels. Cyclin A and B are key cell cycle regulators of G2 to mitosis (G2/M) progression, whereas cyclin E regulates the transition to the S phase. The G2/M checkpoint ensures that cells do not enter mitosis and into contact with chemotherapeutic drugs. The inability of cells to halt their progression at the G2 stage may, therefore, be fatal. The results clearly showed the cyclin-dependent apoptosis effect of the nanoformulations was due to the synergistic effect of introducing all three components simultaneously.

The expression levels of poly ADP ribose polymerase (PARP) and caspase-3/9 are the hallmark sign of cells undergoing apoptosis and with activated cell death pathways. Our results showed that Se@Au@mSiO$_2$/DOX markedly downregulated the expression of PARP and the caspases, indicating a strong interconnection between cell cycle regulating signals and caspase cascade pathways. A cleavage of caspase-3 from a 35-kDa polypeptide to a 17-

Fig. 7 Immunoblot analysis. a Western blot analysis of intrinsic signaling pathways involving tumor suppressor, cell cycle protein, and pro- and antiapoptotic proteins after treatment with different formulations at an equivalent concentration of 0.1 μg/mL of DOX; **b** effect of formulations on FAK, Src, and AKT pathways in MCF-7 and MDA-MB-231 cancer cells, and **c** proposed mechanism. **a** Control, **b** DOX, **c** Nano-Se, **d** Au@mSiO$_2$/DOX (NIR+), **e** Au@mSiO$_2$/DOX (NIR+), **f** Se@Au@mSiO$_2$/DOX (NIR-), and **g** Se@Au@mSiO$_2$/DOX (NIR+)
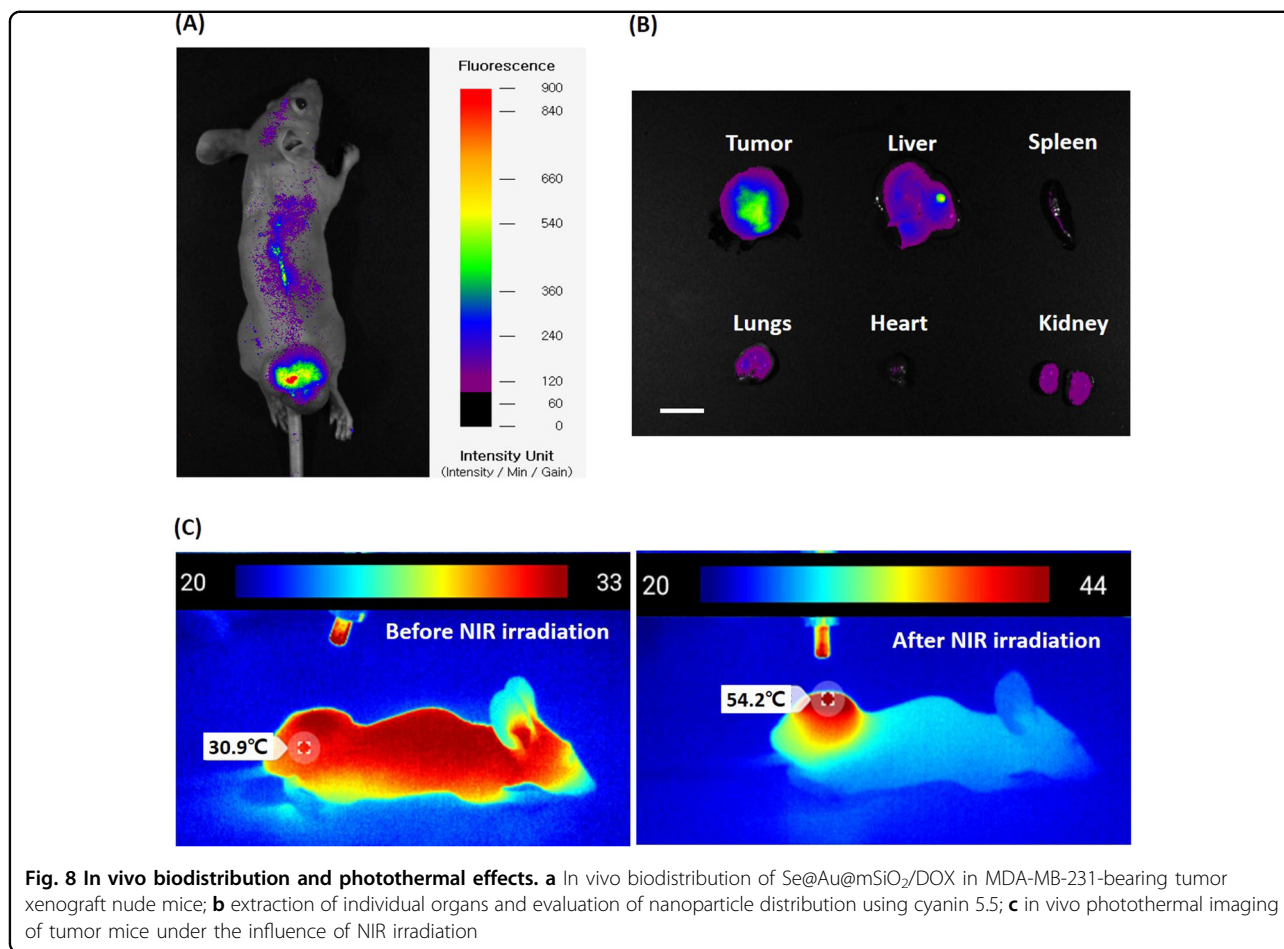
kDa polypeptide was observed, which was further supported by the cleavage of PARP (an enzyme that is activated after DNA damage). Bcl-2 family proteins (major antiapoptotic proteins) are responsible for outer mitochondrial membrane permeability and an important cause of cancer resistance. Its upregulation promotes the survival of cancer cells through the activation of the cytochrome c/Apaf-1 pathway via stabilization of the mitochondrial membrane. Se@Au@mSiO$_2$/DOX remarkably suppressed the expression levels of Bcl-xl, consequently elevating the expression of the pro-apoptotic markers Bid and Bad. This will form pores in mitochondrial membranes, leading to the release of cytochrome C and activation of pro-caspase 9, which will in turn initiate the caspase cascades and apoptosis[40].

Effects of Se@Au@mSiO$_2$/DOX on the Src/FAK/AKT pathways

Intracellular tyrosine kinases, focal adhesion kinase (FAK), and steroid receptor coactivator (Src) form a common intracellular point of convergence in signaling pathways. The upregulation of FAK and/or Src was associated with cancer cell proliferation, survival, migration/invasion, and angiogenesis in cancer patients[41]. The mutually activated FAK/Src complex triggers several downstream signaling pathways, including the Ras-MAPK pathway and the PI3K-AKT cascade, resulting in tumor cell survival/growth. In this study, we investigated the possible role of individual therapeutic molecules in Src/FAK/AKT pathway modulation (Fig. 7b). Free DOX did not have any effect on the expression level of Src, FAK, or pAKT in MDA-MB-231 and MCF-7 cancer cells, indicating its inability to improve therapeutic outcome on its own. Conversely, nano-Se downregulated pAKT and Src/FAK slightly, indicating its effect of ROS-mediated cellular processes. Furthermore, Se@Au@mSiO$_2$/DOX remarkably downregulated/suppressed the expression of all key components, indicating its superior role in promoting cell apoptosis and death. These observations suggest that synergistic combination of anticancer agents and ROS-mediated DNA damage (generated by Se and AuNR) effectively targets/inhibits the Src/FAK/AKT pathways and potentially induces cellular apoptosis (Fig. 7c)[42]. Overall, these results suggest that inhibition of multiple targets, FAK or Src along with AKT, is of great therapeutic importance.

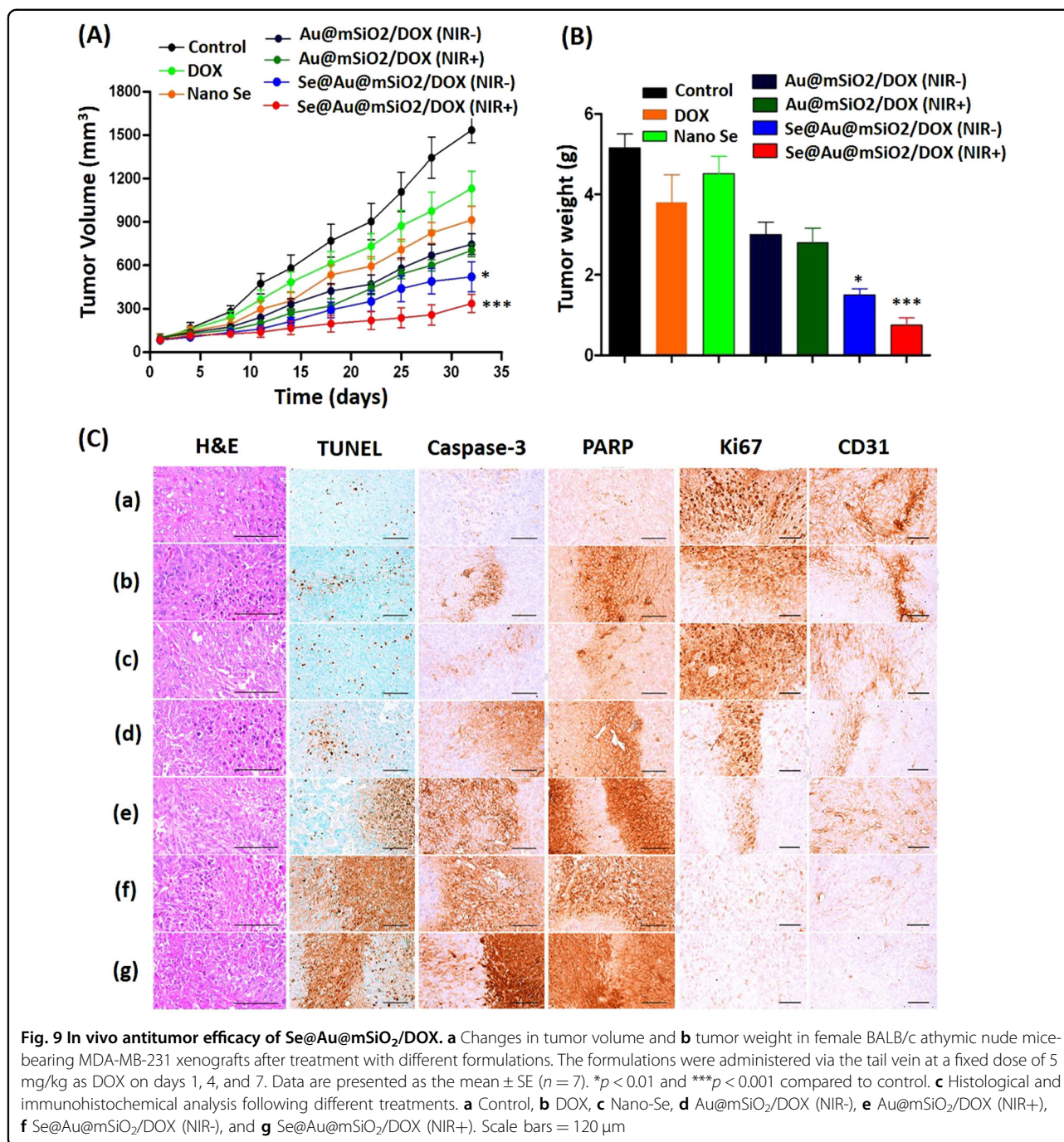### Biodistribution and in vivo antitumor efficacy

In the present study, a remarkable accumulation of nanoparticles was observed in tumor tissues (Fig. 8a). This was likely owing to the enhanced permeation and retention (EPR) effect of the optimized particles, which increased the concentration of the therapeutics in tumor tissues. This excellent antitumor efficacy was mainly

Fig. 8 In vivo biodistribution and photothermal effects. a In vivo biodistribution of Se@Au@mSiO$_2$/DOX in MDA-MB-231-bearing tumor xenograft nude mice; **b** extraction of individual organs and evaluation of nanoparticle distribution using cyanin 5.5; **c** in vivo photothermal imaging of tumor mice under the influence of NIR irradiation

attributed to the monodispersed nanosized particles (~90 nm). We performed a biodistribution analysis of Se@Au@mSiO$_2$ and found greater particle accumulation at 24 h post administration in tumor sites as a result of EPR-based accumulation. The tumor and main organs (the liver, lung, spleen, kidney, and heart) were harvested for ex vivo tissue analysis (Fig. 8b). Notably, ex vivo fluorescence imaging further confirmed the superior tumor accumulation capacity of Se@Au@mSiO$_2$ nanoparticles, showing a significantly greater fluorescence signal in the tumor compared to that in other organs. We have also performed an in vivo photothermal study in the MDA-MB-231 tumor-bearing mice model. At 6 h after treatment via the tail vein, tumors were illuminated with an 808-nm NIR laser for 120 s (3 W/cm^2) (Fig. 8c). During this irradiation, the temperature rapidly increased from 30.9 to 54.2 °C in the focal region, which was a sufficiently high temperature to ablate the tumor cells. The surrounding healthy tissue exhibited a negligible temperature increase of <2 °C. No obvious temperature change was observed in non-irradiated regions of the body. It is likely that Se@Au@mSiO$_2$ nanoparticles accumulated in the

tumor tissue owing to the EPR effects and generated heat under NIR irradiation.

The ability of Se@Au@mSiO$_2$/DOX to inhibit tumor progression was examined using an MDA-MB-231 cancer cell-bearing tumor model. Subcutaneous tumors were developed in the right flank and formulations were administered via intravenous injection. The tumors were irradiated with an NIR laser (808 nm) at a moderate power density of 1.5 W/cm^2 for 10 min. As shown in Fig. 9a, b, Se@Au@mSiO$_2$/DOX (NIR+) exhibited significantly higher tumor growth suppression and delayed tumor progression compared with the other groups, suggesting a synergistic tumor growth inhibition effect. Se@Au@mSiO$_2$/DOX (NIR+) exhibited a three- and fivefold lower tumor volume compared to free DOX and control groups, respectively. Importantly, mice treated with Se@Au@mSiO$_2$/DOX showed continuous tumor regression, with no obvious recrudescence at 15 days after the last drug administration. Au@mSiO$_2$/DOX also could slow down tumor growth to some extent, although it was not as effective as Se@Au@mSiO$_2$/DOX. The survival rate of mice after respective treatment is presented in

Fig. 9 In vivo antitumor efficacy of Se@Au@mSiO₂/DOX. a Changes in tumor volume and **b** tumor weight in female BALB/c athymic nude mice-bearing MDA-MB-231 xenografts after treatment with different formulations. The formulations were administered via the tail vein at a fixed dose of 5 mg/kg as DOX on days 1, 4, and 7. Data are presented as the mean ± SE ($n = 7$). *$p < 0.01$ and ***$p < 0.001$ compared to control. **c** Histological and immunohistochemical analysis following different treatments. **a** Control, **b** DOX, **c** Nano-Se, **d** Au@mSiO₂/DOX (NIR-), **e** Au@mSiO₂/DOX (NIR+), **f** Se@Au@mSiO₂/DOX (NIR-), and **g** Se@Au@mSiO₂/DOX (NIR+). Scale bars = 120 µm

Supplementary Fig. S14. The enhanced antitumor efficacy of Se@Au@mSiO₂/DOX (NIR+) was mainly attributed to the synergistic interaction of chemotherapy, the photothermal reaction, and Se-based apoptotic actions simultaneously. NIR irradiation caused drug release from the mesoporous silica pores, which contributed to additional therapeutic efficacy.

To investigate the possible in vivo mechanisms of the superior antitumor efficacy of Se@Au@mSiO₂/DOX, tumors were extracted and H&E staining was performed (Fig. 9c, Supplementary Table S1). H&E staining revealed remarkable tumor necrosis, marked fragmentation of cells, and loss of membrane integrity in the Se@Au@mSiO₂/DOX (NIR+) treated group. Furthermore, a low tumor cell volume was observed for the optimized groups compared to that reported for the control and individual drug-treated groups. Cellular apoptosis was further confirmed by TUNEL assay. Se@Au@mSiO₂/DOX (NIR+)

and Se@Au@mSiO$_2$/DOX (NIR-)-treated groups showed nearly ten- and eightfold higher cellular apoptosis compared to the control, indicating that the triple-combination strategy mainly contributed to the apoptosis mechanism. Immunohistochemical analysis was performed on extracted tumors to further confirm the antitumor efficacy of the formulations. Mice treated with Se@Au@mSiO$_2$/DOX (NIR+) and Se@Au@mSiO$_2$/DOX (NIR-) showed 11-fold (89.25%) and eightfold (72.54%) higher caspase-3-immunolabeled cells respectively compared to control (9.01%). Accordingly, 13- and tenfold higher PARP-immunolabeled cells were observed for these groups respectively. The expression levels of caspase-3 and PARP are hallmark indication of apoptosis[42,43]. Mitochondrial pores lead to the downstream activation and release of caspase-3, which in turn activates the cleavage of PARP[44,45].

Ki-67 staining was performed to determine the proliferation of primary tumor cells. Over 60% of the cancer cells were Ki-67-positive in the control group, but that proportion decreased to 10.5 and 16% after treatment with Se@Au@mSiO$_2$/DOX (NIR+) and Se@Au@mSiO$_2$/DOX (NIR-), respectively. The anti-angiogenesis effect of the formulations was investigated by CD31 staining. Se@Au@mSiO$_2$/DOX remarkably lowered the number of CD31 + cancer cells versus the other groups. Overall, the antitumor efficacy study and immunohistochemistry suggested that the superior tumor growth suppression and enhanced cellular apoptosis in Se@Au@mSiO$_2$/DOX (NIR+)-treated animals could arise from the synergistic activity of DOX-mediated apoptosis, NIR-mediated PTA, and Se-mediated apoptosis in primary tumor cells.

Acute toxicity in mice tumors

DOX has been a mainstay of cancer chemotherapy. However, its clinical application is often hampered by severe side-effects that negatively affect patient quality of life. The potential systemic side-effects that arise from anticancer drugs and laser irradiation are always a great concern in cancer chemotherapy[46]. Importantly, Se@Au@mSiO$_2$/DOX (with and without NIR irradiation) did not have any effect on mouse body weight, which was in sharp contrast to the 18% body weight loss observed in the DOX-treated group (Fig. 10a). The lack of toxicity in the Se@Au@mSiO$_2$/DOX-treated group indicates the absence of NIR-exposure-induced side-effects despite the pronounced tumoricidal effects. This implies that the implementation of three therapeutic strategies in a single nanocomposite system would achieve optimal therapeutic efficacy without any adverse reactions.

Hematology analysis indicated that Au@mSiO$_2$/DOX and Se@Au@mSiO$_2$/DOX nanoformulations did not affect RBC and PLT counts relative to the control group, indicating the ability of nanoformulations to protect the free drug and Se in the composite system (Fig. 10b). In contrast, PLT, RBC, and HB levels significantly decreased in free DOX and nano-Se administered mice compared to those in the control group. ALT and AST are crucial enzymes in the liver and are common markers for the detection of liver disorders or injury. Free DOX and nano-Se treatment resulted in significantly higher levels of AST and ALT, indicative of serious liver inflammatory disorders. In contrast, enzyme levels were significantly lower in Se@Au@mSiO$_2$/DOX-treated mice (no detectable hepatotoxicity) compared to that of free DOX-treated group and almost similar with the untreated control group, suggesting that the nanocomposite has the potential to overcome drug/Se-based adverse effects. No significant difference in AST and ALT level was found among all formulation groups compared to controls. Likewise, serum BUN and CR are good indicators of kidney damage and nephrotoxicity. Similar to the liver parameters, no significant increase in serum BUN and CR level was observed for Au@mSiO$_2$/DOX and Se@Au@mSiO$_2$/DOX group compared to that of control group, whereas markedly higher levels were observed for the free DOX and nano-Se-treated groups. The result indicates the lack of nephrotoxicity in formulation treated groups.

In addition, drug-related toxicity to major organs was evaluated by H&E staining (Fig. 10c). As seen, free DOX treatment induced serious damage to the liver and heart. Hepatic lesions were observed with severe atrophy of hepatic cells. Acute cellular swellings in the liver were observed, and the mean hepatocyte diameter for the DOX-treated group was $32.26 \pm 2.48\,\mu m$ compared to $19.18 \pm 1.14\,\mu m$ in the control group. Similarly, fragmentation and pathological changes in the heart (myocardial degeneration) and breaking of lung fibers were observed in the DOX-treated animal group. However, no noticeable sign of organ damage or toxicity was observed after treatment with Se@Au@mSiO$_2$/DOX ($\pm$NIR irradiation) suggesting that drug was effectively encapsulated in the nanocarrier and allowed for long-term administration owing to controlled release behavior. Furthermore, NIR irradiation did not cause any adverse effects to normal tissues. The ability of the nanocomposite to significantly reduce organ damage without compromising its therapeutic efficacy is of great clinical potential. Overall, the hematology and biochemical analysis suggest that the functionalized nanosystem could effectively decrease the adverse effects of chemotherapeutic drugs.

Conclusion

In summary, we describe the fabrication of a Se@Au@mSiO$_2$/DOX multifunctional nanoplatform to incorporate materials with specific chemotherapeutic, chemoprevention, and photoablation/hyperthermia
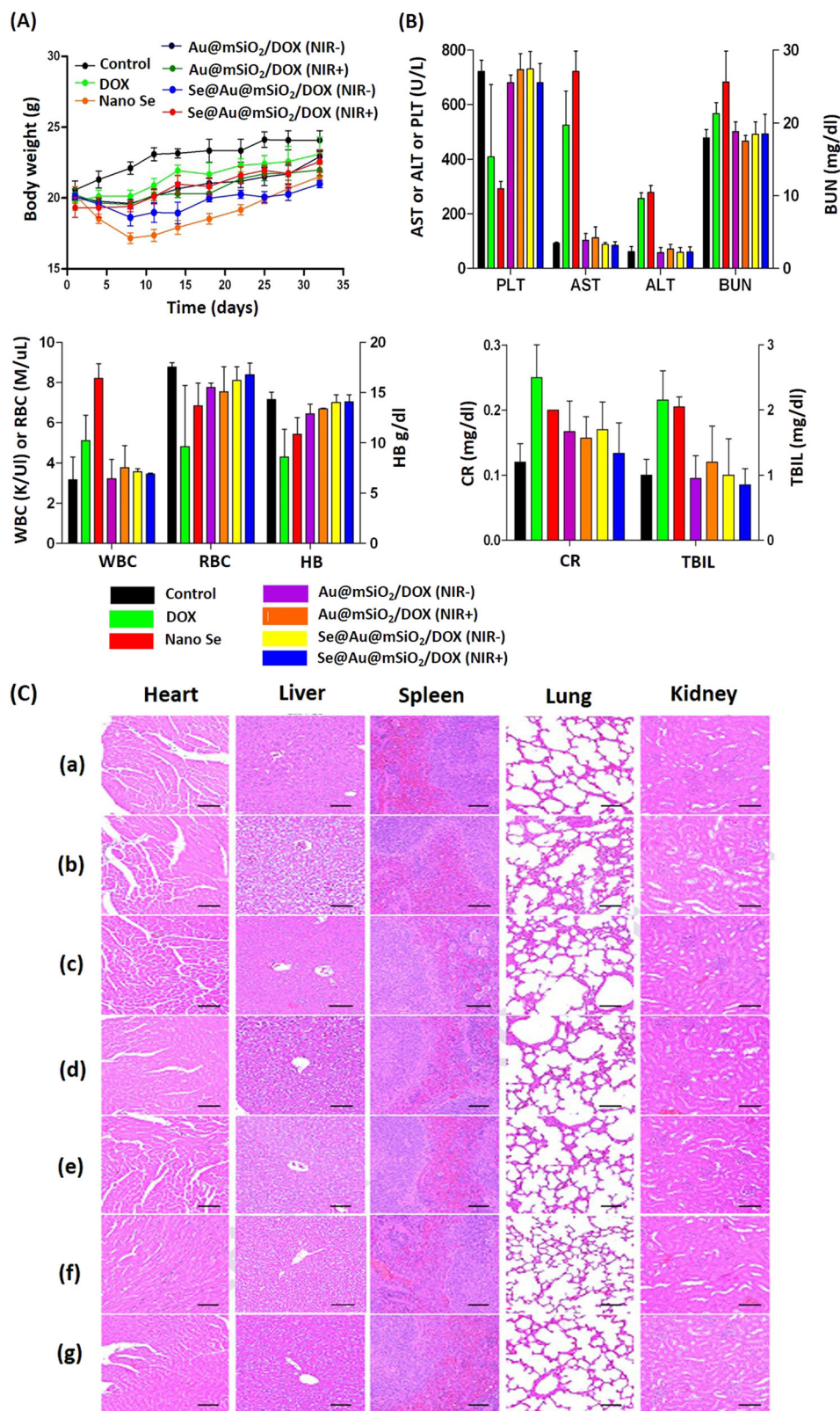
Fig. 10 Toxicity analysis of formulations in major organs. a Changes in body weight; **b** blood biochemical indexes and **c** staining of major organs of female BALB/c athymic nude mice after administration of different formulations. **a** Control, **b** DOX, **c** Nano-Se, **d** Au@mSiO$_2$/DOX (NIR-), **e** Au@mSiO$_2$/DOX (NIR+), **f** Se@Au@mSiO$_2$/DOX (NIR-), and **g** Se@Au@mSiO$_2$/DOX (NIR+). Scale bars = 120 μm

functions, which collectively contribute to enhance anticancer efficacy in multidrug-resistant breast cancers. To the best of our knowledge, this report is the first example of a combination therapy using nano-Se, PTA, and chemotherapy in cancer treatment. This strategy brings new horizons for cancer therapy and opens a new area for the application of multi-metallic NPs and chemotherapeutic drugs. We have demonstrated for the first time that the triple-combination-based nanosized Se@Au@mSiO$_2$/DOX particles could effectively accumulate in the tumor, and the release of therapeutic cargo could be remotely manipulated by mild NIR irradiation. The synergistic nanocomposite system notably enhanced the cell killing effect and a mechanistic investigation revealed that Se@Au@mSiO$_2$/DOX inhibited tumor cell growth through cell cycle arrest and induction of apoptosis via suppression of the Src/FAK/AKT signaling pathways. The synergistic Se-photothermal-chemotherapy combination exhibited significant tumor growth suppression and delayed tumor progression in vivo. No noticeable sign of organ damage or toxicity was observed after treatment with Se@Au@mSiO$_2$/DOX (NIR+), which was further supported by hematology and biochemical analyses. These results imply that Se@Au@mSiO$_2$/DOX has promising potential for the clinical treatment of metastatic breast cancers with little or no adverse effects.

Author details
[1]College of Pharmacy, Yeungnam University, 214-1, Dae-dong, Gyeongsan 712-749, Republic of Korea. [2]Department of Medicine, Center for Ultrasound Molecular Imaging and Therapeutics, University of Pittsburgh, Pittsburgh, PA 15213, USA. [3]Gachon Institute of Pharmaceutical Sciences, Gachon University, Incheon 406-840, Republic of Korea. [4]School of Pharmacy, SungKyunKwan University, 300 Cheoncheon-dong, Jangan-gu, Suwon 440-746, Republic of Korea. [5]College of Korean Medicine, Daegu Haany University, Gyeongsan 712-715, Republic of Korea. [6]College of Pharmacy, Institute of Pharmaceutical Science and Technology, Hanyang University, 55, Hanyangdaehak-ro, Sangnok-gu, Ansan 426-791, Republic of Korea

Conflict of interest
The authors declare that they have no conflict of interest.

Publisher's note
Springer Nature remains neutral with regard to jurisdictional claims in published maps and institutional affiliations.

References
1. Ferlay, J. et al. Estimates of worldwide burden of cancer in 2008: GLOBOCAN 2008. *Int. J. Cancer* **127**, 2893–2917 (2010).
2. Yager, P. et al. Microfluidic diagnostic technologies for global public health. *Nature* **442**, 412–418 (2006).
3. Peer, D. et al. Nanocarriers as an emerging platform for cancer therapy. *Nat. Nanotechnol.* **2**, 751–760 (2007).
4. Du, Q. et al. Synergistic anticancer effects of curcumin and resveratrol in Hepa1-6 hepatocellular carcinoma cells. *Oncol. Rep.* **29**, 1851–1858 (2013).
5. Qiu, L. et al. A cell-targeted, size-photocontrollable, nuclear-uptake nanodrug delivery system for drug-resistant cancer therapy. *Nano Lett.* **15**, 457–463 (2014).
6. Rayman, M. P. The importance of selenium to human health. *Lancet* **356**, 233–241 (2000).
7. Hu, H. et al. Methylseleninic acid enhances taxane drug efficacy against human prostate cancer and down-regulates antiapoptotic proteins Bcl-XL and surviving. *Clin. Cancer Res.* **14**, 1150–1158 (2008).
8. Sun, D. et al. The effects of luminescent ruthenium (II) polypyridyl functionalized selenium nanoparticles on bFGF-induced angiogenesis and AKT/ERK signaling. *Biomaterials* **34**, 171–180 (2013).
9. Liu, W. et al. Selenium nanoparticles as a carrier of 5-fluorouracil to achieve anticancer synergism. *ACS Nano* **6**, 6578–6591 (2012).
10. Fakih, M., Cao, S., Durrani, F. A. & Rustum, Y. M. Selenium protects against toxicity induced by anticancer drugs and augments antitumor activity: a highly selective, new, and novel approach for the treatment of solid tumors. *Clin. Colorectal Cancer* **5**, 132–135 (2005).
11. Zhang, J., Wang, X. & Xu, T. Elemental selenium at nano size (Nano-Se) as a potential chemopreventive agent with reduced risk of selenium toxicity: comparison with se-methylselenocysteine in mice. *Toxicol. Sci.* **101**, 22–31 (2008).
12. Ramasamy, T. et al. Smart chemistry-based nanosized drug delivery systems for systemic applications: A comprehensive review. *J Control. Release* **258**, 226–253 (2017).
13. You, J. et al. Effective photothermal chemotherapy using doxorubicin-loaded gold nanospheres that target EphB4 receptors in tumors. *Cancer Res.* **72**, 4777–4786 (2012).
14. Hyvärinen, M. *Ultraviolet Light Protection and Weathering Properties of Wood-polypropylene Composites.* Doctoral Dissertation, *Acta Universitatis Lappeenrantaensis* (2014).
15. Li, X., Takashima, M., Yuba, E., Harada, A. & Kono, K. PEGylated PAMAM dendrimer–doxorubicin conjugate-hybridized gold nanorod for combined photothermal-chemotherapy. *Biomaterials* **35**, 6576–6584 (2014).
16. Huang, X., Jain, P. K., El-Sayed, I. H. & El-Sayed, M. A. Plasmonic photothermal therapy (PPTT) using gold nanoparticles. *Lasers Med. Sci.* **23**, 217–228 (2008).
17. Dykman, L. & Khlebtsov, N. Gold nanoparticles in biomedical applications: recent advances and perspectives. *Chem. Soc. Rev.* **41**, 2256–2282 (2012).
18. Hauck, T. S., Jennings, T. L., Yatsenko, T., Kumaradas, J. C. & Chan, W. C. Enhancing the toxicity of cancer chemotherapeutics with gold nanorod hyperthermia. *Adv. Mater.* **20**, 3832–3838 (2008).
19. You, J., Zhang, G. & Li, C. Exceptionally high payload of doxorubicin in hollow gold nanospheres for near-infrared light-triggered drug release. *ACS Nano* **4**, 1033–1041 (2010).
20. Shen, S. et al. Targeting mesoporous silica-encapsulated gold nanorods for chemo-photothermal therapy with near-infrared radiation. *Biomaterials* **34**, 3150–3158 (2013).
21. DeLisser, H. et al. Vascular endothelial platelet endothelial cell adhesion molecule 1 (PECAM-1) regulates advanced metastatic progression. *Proc. Natl Acad. Sci.* **107**, 18616–18621 (2010).
22. Awasthi, N., Zhang, C., Ruan, W., Schwarz, M. A. & Schwarz, R. E. BMS-754807, a small-molecule inhibitor of insulin-like growth factor-1 receptor/insulin receptor, enhances gemcitabine response in pancreatic cancer. *Mol. Cancer Ther.* **11**, 2644–2653 (2012).
23. Sau, T. K. & Murphy, C. J. Seeded high yield synthesis of short Au nanorods in aqueous solution. *Langmuir* **20**, 6414–6420 (2004).
24. Ramasamy, T. et al. pH sensitive polyelectrolyte complex micelles for highly effective combination chemotherapy. *J. Mater. Chem. B* **2**, 6324–6333 (2014).
25. Ramasamy, T. et al. Layer-by-layer assembly of liposomal nanoparticles with PEGylated polyelectrolytes enhances systemic delivery of multiple anticancer drugs. *Acta Biomater.* **10**, 5116–5127 (2014).

26. Ramasamy, T. et al. Layer-by-layer coated lipid–polymer hybrid nanoparticles designed for use in anticancer drug delivery. *Carbohydr. Polym.* **102**, 653–661 (2014).

27. Ramasamy, T. et al. Chitosan-based polyelectrolyte complexes as potential nanoparticulate carriers: physicochemical and biological characterization. *Pharm. Res.* **31**, 1302–1314 (2014).

28. Zhang, Z., Wang, J. & Chen, C. Near-infrared light-mediated nanoplatforms for cancer thermo-chemotherapy and optical imaging. *Adv. Mater.* **25**, 3869–3880 (2013).

29. Ramasamy, T. et al. Engineering of a lipid-polymer nanoarchitectural platform for highly effective combination therapy of doxorubicin and irinotecan. *Chem. Commun.* **51**, 5758–5761 (2015).

30. Ramasamy, T., Kim, J., Choi, H. G., Yong, C. S. & Kim, J. O. Novel dual drug-loaded block ionomer complex micelles for enhancing the efficacy of chemotherapy treatments. *J. Biomed. Nanotechnol.* **10**, 1304–1312 (2014).

31. Varkouhi, A. K., Scholte, M., Storm, G. & Haisma, H. J. Endosomal escape pathways for delivery of biologicals. *J. Control. Release* **151**, 220–228 (2011).

32. Tran, T. H. et al. Tumor-targeting, pH-sensitive nanoparticles for docetaxel delivery to drug-resistant cancer cells. *Int. J. Nanomed.* **10**, 5249 (2015).

33. Ramasamy, T. et al. Engineering of cell microenvironment-responsive polypeptide nanovehicle co-encapsulating a synergistic combination of small molecules for effective chemotherapy in solid tumors. *Acta Biomater.* **48**, 131–143 (2017).

34. Ramasamy, T. et al. Cationic drug-based self-assembled polyelectrolyte complex micelles: Physicochemical, pharmacokinetic, and anticancer activity analysis. *Colloids Surf. B: Biointerfaces* **146**, 152–160 (2016).

35. Shrestha, R., Elsabahy, M., Florez-Malaver, S., Samarajeewa, S. & Wooley, K. L. Endosomal escape and siRNA delivery with cationic shell crosslinked knedel-like nanoparticles with tunable buffering capacities. *Biomaterials* **33**, 8557–8568 (2012).

36. Meng, H. et al. Use of size and a copolymer design feature to improve the biodistribution and the enhanced permeability and retention effect of doxorubicin-loaded mesoporous silica nanoparticles in a murine xenograft tumor model. *ACS Nano* **5**, 4131–4144 (2011).

37. Suematsu, N., Hosoda, M. & Fujimori, K. Protective effects of quercetin against hydrogen peroxide-induced apoptosis in human neuronal SH-SY5Y cells. *Neurosci. Lett.* **504**, 223–227 (2011).

38. Gorrini, C., Harris, I. S. & Mak, T. W. Modulation of oxidative stress as an anticancer strategy. *Nat. Rev. Drug Discov.* **12**, 931–947 (2013).

39. Broude, E. et al. p21Waf1/Cip1/Sdi1 mediates retinoblastoma protein degradation. *Oncogene* **26**, 6954–6958 (2007).

40. Sundaramoorthy, P. et al. Engineering of caveolae-specific self-micellizing anticancer lipid nanoparticles to enhance the chemotherapeutic efficacy of oxaliplatin in colorectal cancer cells. *Acta Biomater.* **42**, 220–231 (2016).

41. Falck, J., Mailand, N., Syljuåsen, R. G., Bartek, J. & Lukas, J. The ATM–Chk2–Cdc25A checkpoint pathway guards against radioresistant DNA synthesis. *Nature* **410**, 842–847 (2001).

42. Ruttala, H. B. et al. Molecularly targeted co-delivery of a histone deacetylase inhibitor and paclitaxel by lipid-protein hybrid nanoparticles for synergistic combinational chemotherapy. *Oncotarget* **8**, 14925 (2017).

43. Ruttala, H. B. et al. Multiple polysaccharide-drug complex-loaded liposomes: A unique strategy in drug loading and cancer targeting. *Carbohydr. Polym.* **176**, 57–66 (2017).

44. Fang, E. F. et al. Trichosanthin inhibits breast cancer cell proliferation in both cell lines and nude mice by promotion of apoptosis. *PLoS ONE* **7**, e41592 (2012).

45. Qin, Y. et al. Cardamonin exerts potent activity against multiple myeloma through blockade of NF-κB pathway in vitro. *Leuk. Res.* **36**, 514–520 (2012).

46. Ramasamy, T. et al. Polypeptide-based micelles for delivery of irinotecan: physicochemical and in vivo characterization. *Pharm. Res.* **32**, 1947–1956 (2015).